






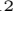








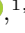





Astrometry and Precise Radial Velocities Yield a Complete Orbital Solution for the Nearby Eccentric Brown Dwarf LHS 1610 b

EVAN FITZMAURICE* ^{1, 2, 3, 4} GUÐMUNDUR STEFÁNSSON ^{5, 6} ROBERT D. KAVANAGH ⁷ SUVRATH MAHADEVAN ^{1, 2}
CALEB I. CAÑAS ^{8, 9} JOSHUA N. WINN ⁶ PAUL ROBERTSON ¹⁰ JOE P. NINAN ¹¹ SIMON ALBRECHT ¹²
J. R. CALLINGHAM ^{13, 7} WILLIAM D. COCHRAN ^{14, 15} MEGAN DELAMER ^{1, 2} SHUBHAM KANODIA ¹⁶
ANDREA S.J. LIN ^{1, 2} MARCUS L. MARCUSSEN ¹² BENJAMIN J. S. POPE ^{17, 18} LAWRENCE W. RAMSEY ^{1, 2}
ARPITA ROY ^{19, 20} HARISH VEDANTHAM ^{7, 21} AND JASON T. WRIGHT ^{1, 2, 22}

¹Department of Astronomy & Astrophysics, Pennsylvania State University, University Park, PA, 16802, USA

²Center for Exoplanets and Habitable Worlds, Pennsylvania State University, University Park, PA, 16802, USA

³Institute for Computational and Data Sciences, The Pennsylvania State University, University Park, PA, 16802, USA

⁴Institute for Computational and Data Sciences Scholar

⁵NASA Sagan Fellow

⁶Department of Astrophysical Sciences, Princeton University, 4 Ivy Lane, Princeton, NJ 08540, USA

⁷ASTRON, Netherlands Institute for Radio Astronomy, Oude Hoogeveensedijk 4, Dwingeloo, 7991 PD, The Netherlands

⁸NASA Postdoctoral Fellow

⁹NASA Goddard Space Flight Center, 8800 Greenbelt Road, Greenbelt, MD 20771, USA

¹⁰Department of Physics & Astronomy, The University of California, Irvine, Irvine, CA 92697, USA

¹¹Department of Astronomy and Astrophysics, Tata Institute of Fundamental Research, Homi Bhabha Road, Colaba, Mumbai 400005, India

¹²Stellar Astrophysics Centre, Department of Physics and Astronomy, Aarhus University, Ny Munkegade 120, 8000 Aarhus C, Denmark

¹³Leiden Observatory, Leiden University, PO Box 9513, 2300 RA, Leiden, The Netherlands

¹⁴McDonald Observatory and Department of Astronomy, The University of Texas at Austin, 2515 Speedway, Austin, TX 78712, USA

¹⁵Center for Planetary Systems Habitability, The University of Texas at Austin, 2515 Speedway, Austin, TX 78712, USA

¹⁶Earth and Planets Laboratory, Carnegie Institution for Science, 5241 Broad Branch Road, NW, Washington, DC 20015, USA

¹⁷School of Mathematics & Physics, University of Queensland, St Lucia, QLD 4072, Australia

¹⁸Centre for Astrophysics, University of Southern Queensland, West Street, Toowoomba, QLD 4350, Australia

¹⁹Space Telescope Science Institute, 3700 San Martin Drive, Baltimore, MD 21218, USA

²⁰Department of Physics and Astronomy, Johns Hopkins University, 3400 N Charles St, Baltimore, MD 21218, USA

²¹Kapteyn Astronomical Institute, University of Groningen, Landleven 12, NL-9747AD Groningen, the Netherlands

²²Penn State Extraterrestrial Intelligence Center, 525 Davey Laboratory, The Pennsylvania State University, University Park, PA, 16802, USA

ABSTRACT

We characterize the LHS 1610 system, a nearby ($d = 9.7$ pc) M5 dwarf hosting a brown dwarf in a 10.6 day, eccentric ($e \sim 0.37$) orbit. A joint fit of the available Gaia two-body solution, discovery radial velocities (RVs) from TRES, and new RVs obtained with the Habitable-zone Planet Finder, yields an orbital inclination of $117.2 \pm 0.9^\circ$ and a mass constraint of $50.9 \pm 0.9 M_J$. This gives LHS 1610 b the second most precise mass of brown dwarfs orbiting M stars within 25pc. We highlight a discrepancy between the Gaia two-body solution eccentricity ($e = 0.52 \pm 0.03$) and that from the RVs ($e = 0.3702 \pm 0.0003$), which requires the astrometric time-series release (Gaia DR4) for further diagnostics. With a flare rate of 0.28 ± 0.07 flares/day from TESS photometry, and a rotation period of 84 ± 8 days, LHS 1610 joins other mid M stars—including Proxima Centauri and YZ Ceti—as nearby mid M dwarfs with flare rates on the higher end for their long rotation periods. These stars are promising candidates for searching for sub-Alfvénic star-companion interactions, raising the question whether LHS 1610 b could be driving the flares on its host star. However, the available TESS photometry is insufficient to confirm or rule out any orbital phase-dependence of the flares. We show that the LHS 1610 system, as

a nearby mid M star with a large, short-period companion, is a promising target to look for evidence of star-companion interactions or aural emission from the brown dwarf at radio wavelengths.

Keywords: stars: low-mass, brown dwarfs: spectroscopic

1. INTRODUCTION

The Gaia mission (Gaia Collaboration et al. 2016) is revolutionizing the field of astrophysics yielding insights into planets, brown dwarfs, and binary stars. The expected detection yield of substellar objects from Gaia—including both exoplanets and brown dwarfs—has been estimated to be thousands to tens of thousands (Lattanzi et al. 2000; Sozzetti et al. 2001; Perryman et al. 2014; Holl et al. 2022). Recently, new detections of substellar objects have been enabled through studying proper motion differences between Hipparcos and Gaia, allowing follow-up confirmation observations through direct imaging and/or radial velocities to gain insights into brown dwarfs (e.g., Brandt et al. 2021; Li et al. 2023) and giant planets (Currie et al. 2023). Previous studies have shown evidence for different formation mechanisms of brown dwarfs and giant planets (Chabrier et al. 2014), e.g., through their different eccentricity distributions (Bowler et al. 2020). Detailed characterization of the orbital parameter distributions of substellar companions—spanning both brown dwarfs and planetary companions—can yield further insights into how these distinct populations of companions form and evolve.

As part of Gaia Data Release 3 (DR3, Gaia Collaboration et al. 2023), 169,277 Gaia two-body solutions were published assuming a single Keplerian model derived from the first 34 months of Gaia observations (Halbwachs et al. 2023). These two-body solutions provide constraints on all orbital elements, including the orbital period, eccentricity, inclination, mass of the companion, and correlation matrices between the parameters assuming a ‘dark’ companion which contributes no light to the photocenter motion measured by Gaia. Most of these solutions are double-star systems, with 1,162 that are likely to be substellar objects analyzed with a dedicated ‘exoplanet’ pipeline (Holl et al. 2022). Recent work by Winn (2022) provided an analysis of planet candidates with Gaia two-body solutions, providing a framework to analyze the two-body solutions along with available radial velocity data, which in some cases highlights good agreement with the Gaia solutions, and sometimes inconsistencies. Recent follow-up observations by Marcussen & Albrecht (2023) further highlight the importance of ground-based observations to confirm and/or rule out false positive scenarios, such as binaries.

Among different stars, nearby M-dwarfs are particularly suitable for detecting substellar companions with Gaia, as they maximize the likelihood of high-precision orbit and mass determination (Sozzetti et al. 2014; Perryman et al. 2014). Around M-dwarfs, Sozzetti et al. (2014) predicted the detection of ~ 100 giant planets at orbits within 3 AU within 30 pc, and $\sim 2,000$ within 100 pc. Such a large sample can place tight constraints on the occurrence rates of substellar companions around M dwarfs, which still remains poorly constrained. Detecting giant planets around M-dwarfs is particularly valuable, as current models do not predict their formation due to the expected inventory of material in the disk being too low (e.g., Miguel et al. 2020; Burn et al. 2021). Such systems, of nearby M stars hosting close-in companions, are also prime candidates to search for possible signatures of star-companion interactions at optical and radio wavelengths to gain insights into the magnetic environments of the orbiting companion (e.g., Callingham et al. 2021; Kavanagh & Vedantham 2023).

In this paper, we perform a detailed characterization of the LHS 1610 system, the second closest M dwarf with a substellar companion and a Gaia two-body solution. The only closer M dwarf system with a substellar companion and Gaia two-body solution is the planetary system GJ 876 (Rivera et al. 2005). LHS 1610 b was originally detected by Winters et al. (2018), before Gaia two-body solutions were available. They characterized it as a mid M dwarf system that hosts a likely brown dwarf in a $P = 10.6$ day eccentric orbit with a minimum mass of $m \sin i = 44.8 \pm 3.2 M_J$ obtained with radial velocities from the TRES spectrograph. After the release of the Gaia two-body solutions, the system was highlighted in Gaia Collaboration et al. (2022), where the Gaia astrometric fit independently confirms the orbit of the brown dwarf, although a joint RV and Gaia two-body solution analysis was not performed. To characterize the LHS 1610 system in further detail, we performed a joint fit of the Gaia two-body solution along with radial velocities, including the RVs from TRES from Winters et al. (2018) and new precise near-infrared RVs from the Habitable-zone Planet Finder (HPF) spectrograph (Mahadevan et al. 2012, 2014) on the 10m Hobby-Eberly Telescope. This allows us to constrain the orbital inclination of the companion, and thereby its mass of $M = 50.9 \pm 0.9 M_J$, confirming that the companion is a brown dwarf. Using

available TESS data, we derive a flare rate for LHS 1610 and compare it to other M star flare rates and their rotation periods from [Pope et al. \(2021\)](#) and [Medina et al. \(2020, 2022\)](#). We find that LHS 1610 resides at the high end of flare rates for its long rotation period for mid M stars, similar to other mid M stars such as Proxima Centauri, YZ Ceti, and GJ 1151. These stars are promising candidates for star-planet interactions due to known companions ([Faria et al. 2022](#); [Anglada-Escudé et al. 2016](#); [Stock et al. 2020](#); [Blanco-Pozo et al. 2023](#)) and radio detections ([Pérez-Torres et al. 2021](#); [Pineda & Villadsen 2023](#); [Triglio et al. 2023](#); [Vedantham et al. 2020](#); [Callingham et al. 2021](#)). This leads us to speculate if the flaring of LHS 1610 is influenced by interactions with its companion. Since additional investigation is necessary to confirm or rule out that scenario, we assess the feasibility of making such a detection. Due to the large size of the short-period companion around a nearby low mass star, we show that the system is particularly favorable for detections of possible star-companion interactions and potential auroral emission from the brown dwarf at radio wavelengths.

This paper is structured as follows. In Section 2, we discuss the parameters of the host star, and we discuss the observations analyzed in Section 3. In Section 4, we discuss our modeling of the Gaia two-body solution and the available RVs, and discuss the accompanying results in Section 5. We place the system in context with other brown dwarf systems in Section 6. In Section 7, we discuss our flare analysis of available TESS data, and energetics of possible star-companion interactions or auroral emission in the system. We conclude with a summary of our findings in Section 8.

2. STELLAR PARAMETERS

To characterize the spectroscopically determined T_{eff} , $[\text{Fe}/\text{H}]$, and $\log g$ parameters, we used the HPF-SpecMatch ([Stefansson et al. 2020](#)) code, which compares an as-observed spectrum with HPF to a library of well-characterized spectra. In doing so, we realized that LHS 1610 is listed in the input library from [Yee et al. \(2017\)](#), with an effective temperature of $T_{\text{eff}} = 3079 \pm 60$ K, metallicity of $[\text{Fe}/\text{H}] = 0.01 \pm 0.08$, and $\log g = 5.04 \pm 0.06$ as originally determined in [Mann et al. \(2015\)](#). As a test, we removed the LHS 1610 spectrum from the library, and we ran it through the HPF-SpecMatch algorithm, recovering consistent values. We elected to adopt the spectroscopically determined measurements as originally reported in [Mann et al. \(2015\)](#). Additionally, the HPF-SpecMatch analysis further confirms a low projected rotational velocity of $v \sin i < 2$ km/s, agreeing with the long rotation period

Table 1. Summary of stellar parameters used in this work.

Parameter	Description	Value	Reference
SpT	Spectral Type	M5	(1)
T_{eff}	Effective Temperature	3079 ± 60 K	(2)
$[\text{Fe}/\text{H}]$	Metallicity	0.01 ± 0.08	(2)
$\log(g)$	Surface gravity (cgs)	5.04 ± 0.06	(2)
R_*	Radius	$0.2007^{+0.0071}_{-0.0063} R_{\odot}$	This Work
Age	Age	$7.0^{+4.5}_{-4.7}$ Gyr	This Work
M_*	Mass	$0.1670 \pm 0.0042 M_{\odot}$	This Work
RV	Systemic RV	43.1 ± 0.1 km s $^{-1}$	This work
d	Distance	$9.6625^{+0.0090}_{-0.0088}$ pc	(3)
ϖ	Parallax	$103.879^{+0.023}_{-0.023}$ mas	(4)
P_{rot}	Rotation Period	84.3 ± 8 days	(1)
$v \sin i$	Rotational Velocity	< 2 km/s	This Work
R_{flare}	Flare Rate ^a	0.28 ± 0.07 day $^{-1}$	This Work
$\ln R_{31.5}$	"High Energy" Flare Rate ^b	-2.51 ± 0.45 day $^{-1}$	This Work

References are: (1) [Winters et al. \(2018\)](#), (2) [Mann et al. \(2015\)](#) (3) [Bailer-Jones et al. \(2018\)](#), (4) Gaia.

[Winters et al. \(2018\)](#) report a rotation period of 84.3 days with a 5-10% error. We adopt a 10% rotation period error.

^aDerived following the methodology in [Pope et al. \(2021\)](#).

^bDerived following the methodology in [Medina et al. \(2020, 2022\)](#).

from [Winters et al. \(2018\)](#) of $P = 84.3$ days which was securely measured using long-term ground-based photometric monitoring from MEarth ([Nutzman & Charbonneau 2008](#); [Irwin et al. 2015](#)).

To obtain constraints on the mass, radius, and age of the system, we performed a fit to the Spectral Energy Distribution (SED) of LHS 1610 using available literature magnitudes of the star using the EXOFASTv2 ([Eastman et al. 2019](#)) code and MESA Isochrones and Stellar Tracks (MIST; [Choi et al. 2016](#); [Dotter 2016](#)) isochrones. As an input for the SED fit, we used informative priors on the spectroscopically determined T_{eff} , $[\text{Fe}/\text{H}]$, and $\log g$ parameters as listed above. In doing so, we obtain a mass of $M = 0.167^{+0.014}_{-0.015} M_{\odot}$, and a radius of $R = 0.2007^{+0.0071}_{-0.0063} R_{\odot}$. As a separate constraint on the stellar mass, we used the M-K relation from [Mann et al. \(2019\)](#), where we find a stellar mass of $M = 0.1670 \pm 0.0042 M_{\odot}$. This agrees with the stellar mass from the SED fit, but is more precise. We elected to adopt the mass from the M-K relation, as the relation has been tightly calibrated for mid-to-late M-dwarfs. Table 1 summarizes our adopted stellar parameters.

3. OBSERVATIONS

3.1. TRES Optical Radial Velocities

We use RVs of LHS 1610 from [Winters et al. \(2018\)](#) which used the Tillinghast Reflector Echelle Spectrograph (TRES). There are a total of 13 RVs that have a median RV uncertainty of 28.3 m/s and span 39 days. The spectra were taken with 900 second exposures in good conditions, and longer in poor conditions. The medium fiber was used with a resolving power of $R \sim 44,000$. The signal-to-noise ratio (SNR) was 15 per pixel at 7150 Angstroms. The RVs were extracted using the pipeline described in [Buchhave et al. \(2010\)](#), and are shown in Panel A of Figure 1.

3.2. HPF Near-infrared Radial Velocities

We acquired precise RVs from the spectra of LHS 1610 using the Habitable-zone Planet Finder spectrograph ([Mahadevan et al. 2012, 2014](#), HPF). HPF is a fiber-fed near-infrared (NIR) spectrograph on the 10 m Hobby-Eberly Telescope (HET, [Ramsey et al. 1998](#)) at McDonald Observatory in Texas, covering the z , Y , and J bands from 810 to 1280 nm at a resolving power of $R \sim 55,000$. To enable precise radial velocities in the NIR, the HPF is temperature-stabilized at the milli-Kelvin level ([Stefansson et al. 2016](#)). We extracted the HPF RVs using a modified version of the SpEctrum Radial Velocity AnaLyzer (SERVAL; [Zechmeister et al. 2018](#)), adapted for HPF following [Metcalf et al. \(2019\)](#) and [Stefansson et al. \(2020\)](#).

In total we obtained 6 HPF observations, which have a median SNR of 158 at 1 micron and a median RV uncertainty of 4.7 m/s. The RVs span 528 days, significantly expanding the total observational baseline. Three of the RV points are the average of two 969 second exposures taken in the same night. Two of the RV points are singular 969 second exposures and the final RV point comes from a spectrum taken with an exposure time of 191 seconds. The RVs are shown in Panel B of Figure 1, and listed in Table 3.

3.3. Gaia Astrometry

As part of Gaia DR3, fits indicating two bodies are reported in the Gaia Archive under the `nss_two_body_orbits`. These two-body fits contain best-fit results for parameters along with a correlation matrix quantifying the correlation between the parameters. We convert the correlation matrix to a covariance matrix using `nsstools`¹ ([Halbwachs et al. 2023](#)). There were 445 astrometric CCD observations used for the Gaia two-body solution fit of LHS 1610 as provided by the Gaia team. Relevant Campbell elements from the

Gaia two-body solution are listed in column 4 of Table 2.

3.4. TESS Photometry

LHS 1610 was observed by the Transiting Exoplanet Survey Satellite (TESS) ([Ricker 2015](#)) in Sectors 42 (2021 August 20-2021 September 16), 43 (2021 September 16-2021 October 12), and 44 (2021 October 12-2021 November 6). In the TESS Input Catalog ([Stassun et al. 2018, 2019](#)), LHS 1610 is listed as TIC 242941982. LHS 1610 shows flares in each TESS Sector; the TESS Sectors with highlighted flares are shown in Appendix A. We determine the flare rate and put this rate in context with other M dwarfs in Section 7.1

4. MODELING OF ASTROMETRY AND RADIAL VELOCITIES

To characterize the system, we compare the results from three different fits: 1) the Gaia two-body solution, 2) a fit of the radial velocities ('RV-only fit'), and 3) a joint fit of both the Gaia two-body solution and the available RVs. For the joint fit, we broadly follow the methodology outlined in [Winn \(2022\)](#). The three models and values are further described below.

4.1. Gaia Two-Body Solution

The two-body solution from the Gaia DR3 `nss_two_body_orbits` table yields constraints on the following parameters:

$$A, B, F, G, e, P, t_p, \varpi \quad (1)$$

where e is eccentricity, P is period, ϖ is the parallax, and t_p is the periastron time referenced to epoch 2016.0 (JD 2,457,389.0). A , B , F , and G are the Thiele-Innes coefficients, where

$$A = a_0(\cos\omega \cos\Omega - \sin\omega \sin\Omega \cos i), \quad (2)$$

$$B = a_0(\cos\omega \sin\Omega + \sin\omega \cos\Omega \cos i), \quad (3)$$

$$F = -a_0(\sin\omega \cos\Omega + \cos\omega \sin\Omega \cos i), \quad (4)$$

$$G = -a_0(\sin\omega \sin\Omega - \cos\omega \cos\Omega \cos i) \quad (5)$$

where a_0 is the semimajor axis of the photocenter converted to milliarcseconds by multiplying by the parallax, ω is the argument of periastron, Ω is the longitude of the ascending node, and i is the inclination. We use the covariance matrix and `nsstools` to use the Thiele-Innes coefficients to yield constraints on ω , Ω , i , and a_0 . [Halbwachs et al. \(2023\)](#) discuss the ranges of these elements and their physical interpretation from the Gaia two-body solution fits. The astrometric fit uniquely constrains the orbital inclination to the physical motion of

¹ <https://www.cosmos.esa.int/web/gaia/dr3-nss-tools>

the orbit, where orbital inclinations between $[0, \frac{\pi}{2}]$ indicate a counterclockwise orbit, while values between $[\frac{\pi}{2}, \pi]$ indicate a clockwise orbit. Due to a degeneracy of π in Ω and ω , the Gaia astrometric orbit fits will have two equivalent possible solutions, and as noted by [Halbwachs et al. \(2023\)](#) the solution provided in the Gaia two-body solution table is the solution where Ω is between $[0, \pi]$ and ω is between $[0, 2\pi]$.

4.2. RV-only fit

For the RV-only fit, we use the following as parameters in the fit:

$$P, t_p, e, \omega, K, \gamma, \quad (6)$$

where K is the radial velocity semi-amplitude, and γ is the radial velocity offset for the spectrograph combined with the stellar RV offset. We fit a new γ for each individual spectrograph. We compute the Keplerian RV model using the `radvel` code ([Fulton et al. 2018](#)). RVs alone allow us to uniquely constrain the value of ω but not the inclination, meaning we cannot determine the true mass of the secondary, only its minimum mass, with just the RVs.

The Doppler likelihood function is:

$$\mathcal{L}_v = \prod_{i=1}^N \frac{1}{\sqrt{2\pi(\sigma_{v,i}^2)}} \exp \left[-\frac{(v_i - v_{i,\text{calc}})^2}{2(\sigma_{v,i}^2)} \right] \quad (7)$$

where v_i is the i -th RV data point, $\sigma_{v,i}$ is the associated uncertainty, and $v_{i,\text{calc}}$ is the i -th model calculated RV. In practice, we take the log of Equation 7 so that we can sum the log value of every i -th step.

To fit the RVs, we use the differential evolution package `PyDE` ([Parviainen 2016](#)) to determine a global maximum-likelihood solution of a Keplerian RV model to the RV observations. We then initialize 100 Markov-Chain Monte Carlo (MCMC) walkers around the global maximum-likelihood solution to perform MCMC sampling of the parameter posteriors using the `emcee` package ([Foreman-Mackey et al. 2013](#)). We ran the walkers for 35,000 steps. After removing a burn-in of 2,000 chains, we assess the convergence of the chains with two metrics. First, we compute the Gelman-Rubin statistic and confirm its value for each parameter is within 1% of unity. This statistic can be unreliable if the chains are not independent (see e.g., discussion in [Hogg & Foreman-Mackey 2018](#)). Therefore, we additionally computed the maximum autocorrelation timescale and adjust the number of chains in the MCMC to be longer than 50 times this value to ensure a sufficient number of independent samples². We find the mean autocorrela-

tion time to be 78 and the maximum to be 109, so from these steps, along with visual inspections of the chains, we conclude that the chains are well-mixed.

4.3. Joint Astrometry and RV fit

For the joint astrometry and RV fit, we use the following as fit parameters,

$$M_*, m_2, e, \omega, \cos i, \Omega, P, t_p, \varpi, \gamma, \quad (8)$$

where M_* is the stellar mass, m_2 is the secondary mass, and $\cos i$ is the cosine of the inclination. Like the RV only fit, we fit individual RV offsets for HPF and TRES.

We use the Gaia likelihood function from [Winn \(2022\)](#), which is:

$$\mathcal{L}_g = \frac{1}{\sqrt{(2\pi)^8 |\det \mathcal{C}|}} \exp \left[-\frac{1}{2} (\Theta^T \mathcal{C}^{-1} \Theta) \right] \quad (9)$$

where \mathcal{C} is the covariance matrix and Θ is the "Gaia deviation vector" which is an 8-column vector of the differences between the Gaia reported value and the calculated value for the following parameters:

$$A, B, F, G, e, P, t_p, \varpi. \quad (10)$$

The total likelihood for each step is the addition of the log values of both the Doppler likelihood and the Gaia likelihood, as shown in Equation 11,

$$\log(\mathcal{L}_{\text{Total}}) = \log(\mathcal{L}_g) + \log(\mathcal{L}_v). \quad (11)$$

Similar to the RV-only fit, we use `PyDE` to find a global maximum-likelihood solution, after which we use `emcee` to perform MCMC sampling of the posteriors. We initialize 100 walkers and run those walkers for 45,000 chains. We removed the first 2,500 chains as burn-in chains. Our Gelman-Rubin statistics are all within 1% of unity. The mean autocorrelation timescale is 178, while the maximum is 282, meaning our chains are well mixed. As mentioned in Sections 4.2 and 4.1, RVs uniquely constrain ω but not the inclination nor Ω , while the astrometry uniquely constrains inclination, but has the π degeneracy for ω and Ω . By jointly fitting the RVs and the astrometric solution, we can constrain all three values and break the degeneracies.

5. RESULTS

Table 2 summarizes the priors and the posteriors from the three models we considered. The results from the final joint-fit are graphically summarized in Figure 1.

5.1. RV-only

First, we compare our results in Table 2 from the RV-only fit (third column) to the values in [Winters et al.](#)

² <https://emcee.readthedocs.io/en/latest/tutorials/autocorr/>

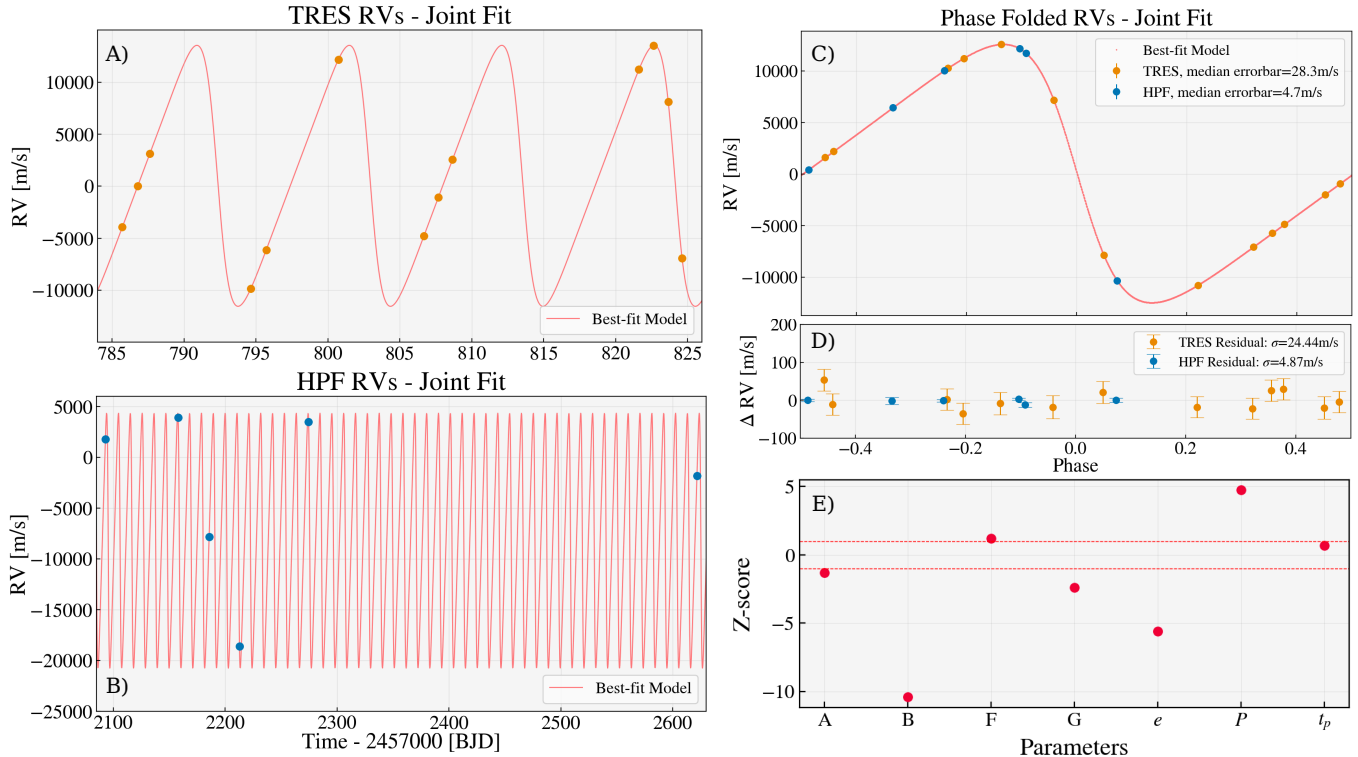


Figure 1. Visualization of joint Gaia-RV fit. **A:** RVs using TRES from [Winters et al. \(2018\)](#), with our best-fit model laid over the points. **B:** Our new RVs using HPF, with the best fit model in red. This shows the significant increase in the observing baseline provided by the additional HPF RVs which span more than 500 days. **C and D:** Phase folded RVs and residuals using the parameters produced by the joint fit. Both sets of RVs are in agreement with the best-fit model. **E:** Z-score comparing the fit values of the Thiele-Innes coefficients A, B, F, and G, as well as the eccentricity, period, and time of periastron to the expected values from Gaia. The red dashed lines indicate 1 sigma. Errors in panels A, B, and C are smaller than the marker size. The RVs are available in a machine readable table with the manuscript.

(2018). The values we obtain are consistent with the values reported in [Winters et al. \(2018\)](#) using only TRES RVs. The additional HPF RVs allow us to significantly improve the precision on multiple parameters including decreasing the orbital period uncertainty by a factor of 140, and the eccentricity is more tightly constrained as $e = 0.37019 \pm 0.0003$ compared to $e = 0.36942 \pm 0.00093$ from [Winters et al. \(2018\)](#). We experimented running fits with individual RV jitter parameters for TRES and HPF that had Jeffreys priors from 0.1 to 100 m/s. This returned Keplerian parameter constraints consistent with the fits with no jitter. The jitter estimates were $1.6^{+9.3}_{-1.3}$ m/s and $4.4^{+8.7}_{-3.9}$ m/s for TRES and HPF, respectively. The modes of the distributions of the jitter values are 0 m/s. From this, we interpret that the RV uncertainties provide an accurate estimate of the total uncertainties and we elect to list the posterior results from the RV-only fit without the jitter values.

5.2. RV-only vs. Gaia Two-Body Solution

Second, we compare our RV-only results to the results from the Gaia two-body solution (fourth column in Ta-

ble 2). Although most parameters show broad consistency between the RV-only solution and the Gaia two-body solution—including the orbital period and time of periastron—we see a discrepancy between the eccentricity from the two-body solution of $e = 0.524 \pm 0.027$, and that of the RV-only fit of $e = 0.37019 \pm 0.00003$.

A few possibilities could explain this discrepancy. First, a third body may be present in the system that could be biasing the astrometry. However, we deem this unlikely as the RV residuals do not exhibit additional structure or trends from the single companion Keplerian fits.

Another possibility could be that the secondary companion is contributing secondary light, breaking the assumption of a dark companion in the Gaia two body solution. To check if this assumption is warranted in the LHS 1610 system, we estimated the flux ratio between the brown dwarf and host star in the Gaia bandpass. Using the Sonora-Bobcat spectral templates ([Marley et al. 2021](#)) for the brown dwarf, PHOENIX stellar spectral templates ([Husser et al. 2013](#)) for the star, and accounting for the transmission curve across the Gaia bandpass,

we estimate the flux ratio in the Gaia bandpass (320–1100 nm) to be negligible (less than 10^{-6}). As such, we do not expect light emitted from the brown dwarf to impact the Gaia solution.

Lastly, the Gaia two-body solution and the associated covariance matrix may not be accurately depicting the shapes of the posteriors of the orbital parameters, but ‘bananas’ and/or other non-linear covariances between different parameters would likely not be accurately estimated using the sampling methodology we used (see further discussion in Winn 2022 and Marcussen & Albrecht 2023).

Without the actual astrometric data, it is difficult to isolate the exact cause of this discrepancy, and we suggest that the joint fit would need to be revisited when the individual Gaia astrometric time-series are released as part of Gaia DR4.

Additionally, we note that the values for ω between the RV-only and the Gaia Two-body solution differ by $\sim 180^\circ$, which is a result of the π degeneracy in ω in the astrometric two-body solution fits (see Section 4.1 and Appendix B of Halbwachs et al. 2023). An important note is that the inclination for Gaia sets the direction of the orbit. Since the inclination is between $[\frac{\pi}{2}, \pi]$ the system orbits in a clockwise direction as observed from Earth. To reflect this, for the joint fit, we placed a uniform prior on $\cos i$ from -1 to 0 (see Table 2).

5.3. Joint RV+Gaia Fit

Finally, the results of the joint fit are shown in the sixth column of Table 2 and the results from the fit are graphically summarized in Figure 1. In panels C and D, we see that both the optical TRES and the NIR HPF RVs fully agree on the RV orbit showing RV residuals with no apparent residual structure. From the joint fit, we find an inclination of $i = 117.19_{-0.91}^{+0.88}$ degrees, which is 24 degrees greater than the value expected by the Gaia two-body solution. From this inclination we constrain the true mass of the brown dwarf to be 50.9 ± 0.9 Jupiter masses. We see from Table 2 that the joint-fit eccentricity fully agrees with the RV-only eccentricity, suggesting it is primarily being constrained by the RVs.

As noted previously, astrometric fits have two solutions and Gaia reports the solution where Ω is bound to $[0, \pi]$ and ω to $[0, 2\pi]$. The RV information breaks the π degeneracy and informs us of the correct solution. Gaia reports $\Omega = 162.6$ degrees and $\omega = 271.4$ degrees. Our joint fit produces $\Omega = -14.9$ degrees and $\omega = 89.31$ degrees. Our fit matches both the astrometric fit, and the RVs.

Figure 1E, shows a Z-score panel. The Z-score for a given parameter is calculated as

$$\text{Z-score} = \frac{x_1 - x_2}{\sigma_{x_2}} \quad (12)$$

where x_1 and x_2 are two different measurements of the same parameter and σ_{x_2} is the error on the x_2 measurement. Our Z-scores are the differences between the joint-fit and the Gaia-only posterior values, scaled by the Gaia-only uncertainties for the Thiele-Innes coefficients, e , P , and t_p . Our B value is smaller by ~ 10 sigma, e is smaller by ~ 5 sigma, and P is larger by ~ 5 sigma. From the covariance matrix, B has the strongest covariance with e compared to the other Thiele-Innes coefficients. As such, we suspect the explanation for the strong shift in eccentricity leads to this dramatic difference for B and the inclination. Further investigations into those correlations require access to the raw Gaia astrometry, which will be available with the Gaia DR4 release.

6. COMPARISON TO OTHER BROWN DWARF M DWARF SYSTEMS

LHS 1610 b joins a small but growing number of nearby brown dwarfs with precisely measured dynamical masses. Figure 2 puts LHS 1610 b in context with other known brown dwarf M-dwarf (BD-M) systems drawn from a compilation of objects with masses between 13 and 80 Jupiter masses from the NASA Exoplanet Archive (Akeson et al. 2013), the Exoplanet.EU catalog, and the literature.

The top panel of Figure 2 shows the brown dwarf mass as a function of distance of the system from Earth where the points are color coded by the host star mass. We cut out systems that have a mass precision worse than 33%. We find LHS 1610 b to be the third closest BD-M system within our mass precision constraint. The other two more nearby targets are: GJ 229 B (Brandt et al. 2021) and Scholz’s Star B (Dupuy et al. 2019). Brandt et al. (2021) note that GJ 229 B is in tension with evolutionary models, as an object of its mass cannot cool to its luminosity within a Hubble time, suggesting it could instead be an unresolved binary (Howe et al. 2023). If GJ 229 B is a binary, LHS 1610 b would become the most precisely known brown dwarf mass in a BD-M binary within 25 parsecs.

By a statistical analysis of the brown dwarf population around FGK stars, Ma & Ge (2014) suggested that the brown dwarf population can be split into two regimes: the low mass regime ($M < 42.5M_{\text{Jup}}$) with an eccentricity distribution similar to gas giant planets, and a high

Table 2. Results from the three fits considered in this work. Priors labeled \mathcal{U} are uniform within those bounds. Those with \mathcal{N} are Normal priors with the first value being the mean and the second value being the standard deviation of the Normal distribution. Priors with only a numerical value are fixed at that value. .

Parameter	RV-only Prior	RV-only fit	Gaia Two-Body Solution	Joint Prior	Joint Fit
M_* (M_\odot)	-	-	-	$\mathcal{N}(0.1671, 0.004)$	$0.1672^{+0.0041}_{-0.0041}$
m_2 (M_{Jup})	-	-	-	$\mathcal{U}(1.0, 100.0)$	$50.9^{+0.9}_{-0.9}$
$\cos i$	-	-	-	$\mathcal{U}(-1.0, 0.0)$	$-0.457^{+0.014}_{-0.014}$
i ($^\circ$)	-	-	$92.8^{+1.9}_{-1.9}$	-	$117.19^{+0.88}_{-0.91}$
K (m/s)	$\mathcal{U}(100000., 200000.)$	$12534.6^{+9.7}_{-9.6}$	-	-	$12540.7^{+9.7}_{-9.7}$
e	$\mathcal{U}(0.0, 0.9)$	$0.37019^{+0.0003}_{-0.0003}$	$0.524^{+0.027}_{-0.027}$	$\mathcal{U}(0.0, 0.9)$	$0.37004^{+0.0003}_{-0.0003}$
ω (degs)	$\mathcal{U}(0.0, 360.0)$	$89.22^{+0.14}_{-0.14}$	$271.4^{+2.9}_{-2.9}$	$\mathcal{U}(0.0, 360.0)$	$89.31^{+0.14}_{-0.14}$
Ω (degs)	-	-	$162.6^{+1.5}_{-1.5}$	$\mathcal{U}(-180.0, 180.0)$	$-14.9^{+0.82}_{-0.81}$
t_{peri} (days) ^a	$\mathcal{U}(-6.0, 6.0)$	$0.7107^{+0.0031}_{-0.0031}$	$0.61^{+0.15}_{-0.15}$	$\mathcal{U}(-6.0, 6.0)$	$0.7119^{+0.0031}_{-0.0031}$
P (days)	$\mathcal{U}(10.5638, 10.6198)^b$	$10.594724^{+0.00002}_{-0.00002}$	$10.5885^{+0.0013}_{-0.0013}$	$\mathcal{U}(10.5638, 10.6198)^b$	$10.594733^{+0.00002}_{-0.00002}$
ϖ (mas)	-	-	-	$\mathcal{N}(103.879, 0.023)$	$103.881^{+0.023}_{-0.023}$
γ_{TRES} (m/s)	$\mathcal{U}(-2000.0, 2000.0)$	$945.2^{+8.2}_{-8.2}$	-	$\mathcal{U}(-2000.0, 2000.0)$	$944.0^{+8.2}_{-8.2}$
γ_{HPF} (m/s)	$\mathcal{U}(-17000.0, 17000.0)$	$-8244.1^{+3.2}_{-3.2}$	-	$\mathcal{U}(-17000.0, 17000.0)$	$-8245.7^{+3.2}_{-3.2}$
ε	0	-	0	-	-
a_0 (mas)	-	-	$1.391^{+0.037}_{-0.037}$	-	$1.325^{+0.011}_{-0.011}$
A (mas)	-	-	$-0.053^{+0.067}_{-0.067}$	-	$-0.14^{+0.01}_{-0.01}$
B (mas)	-	-	$-0.055^{+0.051}_{-0.051}$	-	$-0.589^{+0.023}_{-0.023}$
F (mas)	-	-	$-1.327^{+0.037}_{-0.037}$	-	$-1.282^{+0.012}_{-0.012}$
G (mas)	-	-	$0.418^{+0.035}_{-0.035}$	-	$0.334^{+0.018}_{-0.018}$

^aFor the periastron time, we follow the Gaia convention where the periastron time is $t_{\text{peri}} = 2457389.0 + t_p$, where t_p is the value listed in the table above.

^bThis prior is a ± 10 sigma window of the Winters et al. (2018) period of 10.5918 ± 0.0028 days. This encompasses the period from the Gaia two-body solution.

mass regime with an eccentricity distribution similar to binary stars. With a mass of $50.9 \pm 0.9 M_J$, LHS 1610 b is formally in the high-mass regime discussed in Ma & Ge (2014), and therefore could have formed through molecular cloud fragmentation, similar to a binary stellar companion, as opposed to forming similar to a giant planet via gravitational instability or core-accretion. However, in reality, the boundary between the two regimes is not exact, and is rather characterized by a ‘depletion region’ between $35 - 55 M_J$ as discussed by Ma & Ge (2014), where short-period ($P < 100$ days) brown dwarfs are observed to be intrinsically rare. From its mass alone it is unclear which formation pathway LHS 1610 b would be more compatible with. Since this study was performed on a sample of FGK stars, it may not be directly applicable to our BD-M dwarf binary. More discoveries of brown dwarfs orbiting M-dwarfs will allow us to re-analyze the same distributions shown in Ma & Ge (2014) and determine if the split in populations continues for lower primary masses.

The faint points in Figure 2 highlight that Gaia is yielding a number of additional candidate BD-M systems, allowing further insights into their occurrence rates and eccentricity distribution. However, as highlighted in this work as well as in Halbwachs et al. (2023),

Winn (2022) and Marcussen & Albrecht (2023), precise RV follow-up observations are necessary to confirm those systems and to rule out false positive scenarios.

To further investigate LHS 1610 b’s association with the planet or binary star formation pathways, Figure 2B compares the eccentricity and period of LHS 1610 b to other brown dwarfs. We see that LHS 1610 b has the highest eccentricity for systems with periods $< 10,000$ days. Because of the short-period and non-zero eccentricity, we may expect that tides will circularize LHS 1610 b’s orbit (e.g., Mazeh 2008; Damiani & Díaz 2016). The companion will be circularized if its orbital period is less than the circularization period. M dwarf binaries have an observed circularization period of ~ 10 days (Udry et al. 2000; Mayor et al. 2001), while Sun-like binaries are ~ 10 -12 days (Duquennoy & Mayor 1991; Meibom & Mathieu 2005; Raghavan et al. 2010). The dashed line in Figure 2B indicates the maximum eccentricity a companion of a given period could have without experiencing tidal effects if the circularization period is 10 days. (eq. 3, Halbwachs et al. 2005). With a period of $P = 10.6$ days and an eccentricity of $e = 0.37$, LHS 1610 b is inconsistent with both the aforementioned circularization period trends. Instead, LHS 1610 b fits a shorter circularization period of ~ 8 days, more in-line

with the circularization periods of a few days observed for giant exoplanets (Halbwachs et al. 2005; Pont et al. 2011; Bonomo et al. 2017).

We estimate the circularization timescale to compare with our coarse estimate of the age of $7.0_{-4.7}^{+4.5}$ Gyr from the SED analysis. We use the Sonora-Bobcat models (Marley et al. 2021), to estimate the radius of the brown dwarf based on the mass and an age between 0.5 and 12 Gyr. Using the solar metallicity models, at 0.5 Gyr we find a radius of $0.986R_J$, and at 12 Gyr, $0.785R_J$. We estimated the circularization timescale of the brown dwarf using Equations 1 and 2 from Jackson et al. (2008) and presented in Cañas et al. (2022) as:

$$\frac{1}{\tau_e} = \frac{1}{\tau_{e,*}} + \frac{1}{\tau_{e,BD}}, \quad (13)$$

$$\frac{1}{\tau_{e,*}} = a_{BD}^{-13/2} \frac{171}{16} \sqrt{\frac{G}{M_*}} \frac{R_*^5 M_{BD}}{Q_*}, \quad (14)$$

$$\frac{1}{\tau_{e,BD}} = a_{BD}^{-13/2} \frac{63}{4} \sqrt{GM_*^3} \frac{R_{BD}^5}{Q_{BD} M_{BD}}, \quad (15)$$

where τ_e is the circularization timescale, $\tau_{e,*}$ is the timescale contribution from the star and $\tau_{e,BD}$ is the timescale contribution from the brown dwarf. The parameters a_{BD} , M_* , M_{BD} , R_* , R_{BD} , Q_* , Q_{BD} are the semimajor axis of the brown dwarf, the stellar host mass, the brown dwarf mass, the radius of the stellar host, the brown dwarf radius, the tidal dissipation factors of the stellar host and brown dwarf, respectively. We assume a value of $Q_* = 10^7$ based on modeling done in Gallet et al. (2017) and $Q_{BD} = 10^5$ as inferred for Jupiter (Goldreich & Soter 1966; Lainey et al. 2009; Lainey 2016). We assume the tidal dissipation factors remain constant over time, but in reality this factor will change as the star and brown dwarf evolve. For the 0.5 Gyr and 12 Gyr age assumptions, we obtain circularization timescales of 240 Gyr and 720 Gyr, respectively. The high circularization timescale we obtain in both cases suggests the system is not circularizing.

Additionally, we estimated the timescale for tidal synchronization using the equation from Rasio et al. (1996); Guillot et al. (1996),

$$\tau_s = Q_{BD} \left(\frac{R_{BD}^3}{GM_{BD}} \right) \omega_{BD} \left(\frac{M_{BD}}{M_*} \right)^2 \left(\frac{a_{BD}}{R_{BD}} \right)^6, \quad (16)$$

where ω_{BD} is the primordial rotation rate of the brown dwarf. We again assume a value of $Q_{BD} = 10^5$ and a primordial rotation rate (ω_{BD}) of 10 hours (1.7×10^{-4} cycles per second), equal to that of Jupiter. For the 0.5 Gyr and 12 Gyr age assumptions, we obtain synchronization timescales of ~ 7 Gyrs and ~ 15 Gyrs, respectively. These shorter timescales are similar to our course

age estimate of the system, suggesting that the brown dwarf may be experiencing tidal synchronization and/or is already fully tidally locked. We note that the exact value is strongly dependent on the assumed primordial spin rate and tidal dissipation factor.

7. PROSPECTS FOR STAR-COMPANION INTERACTIONS

Companions that closely orbit their host stars are expected to be able to magnetically interact with their host in a way that, in some cases, modulates stellar activity. Such modulations can result in enhanced X-ray and flaring activity (Lanza 2018; Ilin & Poppenhaefer 2022), radio emission (Callingham et al. 2021; Kavanagh & Vedantham 2023; Zarka et al. 2001; Zarka 2007) or chromospheric spots (Shkolnik et al. 2005), all of which would constitute signatures of magnetic star-companion interactions. However, the magnitudes and scaling relationships of these interactions remain poorly constrained, and detections of objects compatible with such interactions are valuable laboratories to study such models. Due to its sub 10 pc distance, the large size of the companion, and the short orbital period of the brown dwarf, LHS 1610 is a promising target for searching for possible evidence of star-companion interactions. We discuss this possibility in further detail in the following subsections.

7.1. Investigation of Potential Companion-induced Flaring

One way to look for evidence of star-companion interactions is through looking for evidence of phase dependence of flaring (e.g., Lanza 2018; Ilin & Poppenhaefer 2022) and/or orbital phase dependent variations in stellar activity indicators (e.g., Shkolnik et al. 2005), especially at orbital phases close to periastron. Examining the 6 visits of HPF observations, we see no evidence of emission in the Ca II IRT activity indicators, and detect no hints of modulation as a function of orbital phase, and conclude that the star is not chromospherically active.

To constrain the possibility of flare-induced interactions in LHS 1610, we examined the three available Sectors of TESS data of LHS 1610. To detect flares, we used the `stella` code (Feinstein et al. 2020a,b) which leverages a set of trained Convolutional Neural Networks (CNN) to identify flares. To estimate a flare rate, we follow the methods outlined in Pope et al. (2021) and Medina et al. (2020), which we summarize briefly here. Using `stella`, we analyze the TESS 2 minute cadence Presearch Data Conditioning Single-Aperture Photometry (PDCSAP) light curves using the `lightkurve` package (Lightkurve Collaboration et al. 2018) and apply a

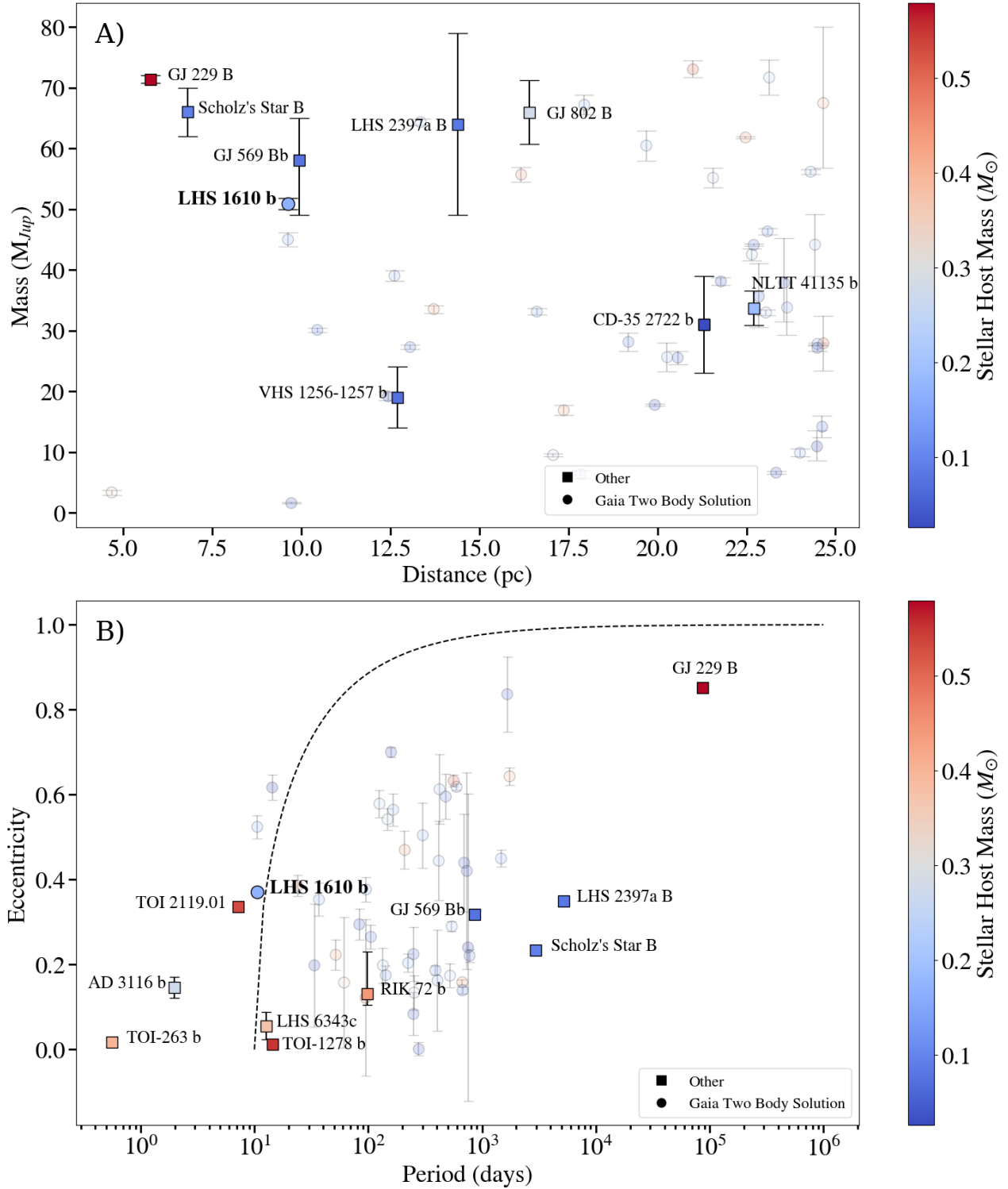


Figure 2. LHS 1610 b in context with other brown dwarfs orbiting M stars (BD-M systems). The colored points are confirmed BD-M star systems drawn from the NASA Exoplanet Archive, the Exoplanet.EU catalog, and the literature. The fainter points show candidate BD-M systems from Gaia two-body solutions within 25pc. Some errors are smaller than the marker size. **Top (A):** Brown dwarfs masses (better than 3σ) as a function of distance from Earth colored by the host star mass. LHS 1610 b is the 3rd most nearby BD-M system with a precise mass measurement. **Bottom (B):** Same as above, but showing eccentricity as a function of orbital period in days. LHS 1610 b is one of the shortest period BDs orbiting an M dwarf, and is the most eccentric in our sample besides GJ 229 B. The dashed line shows the expected eccentricity at a given period for a circularization period of 10 days.

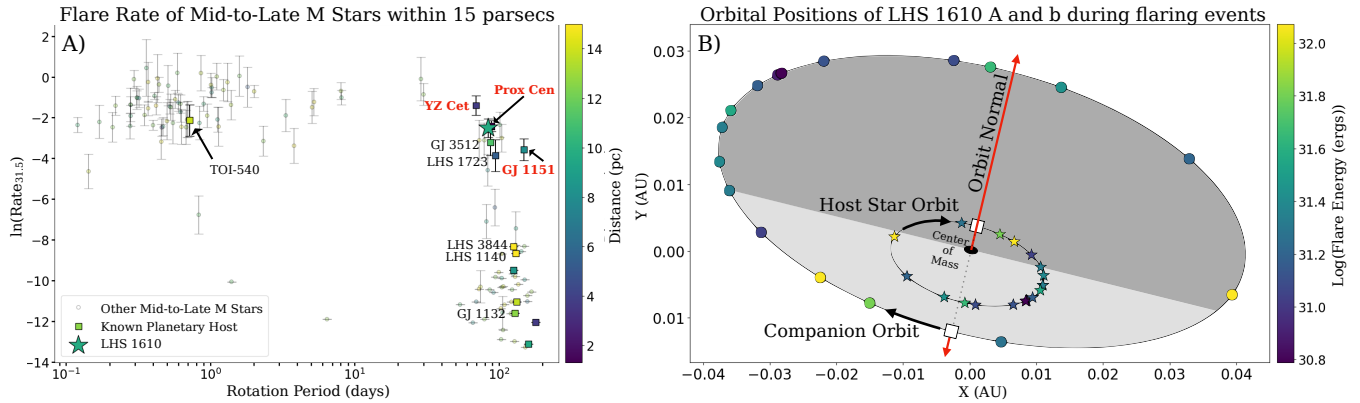


Figure 3. M Dwarf Flare Rates (A): Log flare rate of flares with energies above the 3.16×10^{31} ergs energy threshold discussed in Medina et al. (2022) as a function of stellar rotation period. Points are color coded by distance to Earth. LHS 1610 is highlighted with the star. Systems with substellar companions are highlighted with the black labels. Systems with published radio detections are highlighted in red. LHS 1610 joins a group of systems with high flare rates and long rotation periods. **LHS 1610 flare orbital locations (B):** Orbit visualization of the LHS 1610 b (outer ellipse) and its host star (inner ellipse) around the common center of mass using the joint Gaia-RV parameters from Table 2. The orbit is inclined $\sim 117^\circ$ and the orbital direction is clockwise. The red vector denotes the orbit normal, and the periastron location is highlighted with the dotted line between the white squares. Locations of flares are highlighted twice per flare with the colored points: with a star/circle marker at the corresponding star/companion location. We do not see statistically significant evidence for a phase-dependence of flare locations. A table with flare parameters (times, energies, phases) is available.

flare probability threshold of 0.6. To remove false positives, we follow Pope et al. (2021) and remove flares with a) fractional amplitudes less than 3 times the standard deviation of a 400-min smoothed light curve, or b) rise+fall times less than 4 minutes (two TESS cadences). After this step, sectors are reviewed by eye to add or remove any flares that were clearly misidentified.

Using this methodology, we detected a total of 17 flares: 4 in Sector 42, 6 in Sector 43, and 7 in Sector 44 (see Figure 6 in the Appendix). From this, we estimate a flare rate of 0.28 ± 0.07 flares per day estimated using the total number of flares across the observing baseline covered by all three sectors. We estimate the 1σ uncertainty using a two-sided Poisson confidence interval. This flare rate is high given the star's rotation period when compared to a sample of nearby M stars with confirmed radio emission presented in Pope et al. (2021). LHS 1610 b has a flare rate similar to the M stars DO Cep and LP 259-39 which have substantially more rapid rotation periods of 0.41 days and 1.7 days, respectively.

To further investigate the possibility of flare-induced interactions, in Figure 3A we compare the flare rate of LHS 1610 as a function of rotation period from the volume-complete sample of mid-to-late M dwarfs within 15pc from Medina et al. (2020) and Medina et al. (2022). By replicating their energy cutoff, completeness correction, and flare energy distribution, we see that LHS 1610 has a flare rate on the high end for its stellar rotation period of $P_{\text{rot}} = 84.3 \pm 8$ days. The natural log of this

flare rate is $\ln(R_{31.5}) = -2.51 \pm 0.45$ flares day^{-1} for flares above an energy of 3.16×10^{31} ergs. We refer to this as the "high energy" flare rate. In Figure 3A, we highlight systems with confirmed substellar companions from the NASA Exoplanet Archive. Additionally, in Figure 3A we label in red systems with published radio detections that have been highlighted as potentially compatible with star-planet interactions including GJ 1151 (Vedantham et al. 2020; Callingham et al. 2021), Proxima Cen (Pérez-Torres et al. 2021), and YZ Ceti (Pineda & Villadsen 2023; Trigilio et al. 2023). Figure 3A shows that LHS 1610 joins those systems as an inactive, nearby M star with a longer rotation period, high optical flare rate, and a known companion. These similarities lead us to speculate that the brown dwarf may be inducing flares on LHS 1610. We evaluate the feasibility of observations that could be used to gain further insights into such interactions in the next section.

We further visualize the position of the flares in the orbit of LHS 1610 in Figure 3. Each flare along with its flare energy are shown both on the host star orbit (star markers), as well as the position of the companion (circles). The flare energies are estimated following the same methodology as Medina et al. (2020). From Figure 3, we do not see any clear phase-dependent preference, including no clear preference for flaring close to periastron. In the half of the orbit encompassing periastron (phase values between -0.25 and 0.25 in Panel D of Figure 6) we find 9 flares, which is consistent with the expectation of 8.6 ± 2.2 flares given our flare rate, sug-

gesting there is no preference for flaring near periastron. We note that due to the low number of 17 flares detected, the Poisson counting uncertainties on expected numbers of flares remain high. As such, additional flare monitoring to increase the total number of flare detections would be needed to provide conclusive evidence of any flare dependence in the system.

Lastly, brown dwarfs are known to have flares at comparable strengths to those observed around M stars (Gizis et al. 2017; Paudel et al. 2020), and some or all of the flares seen in the TESS photometry could be attributed to the brown dwarf. However, flaring brown dwarfs are generally young (< 1 Gyr), and have spectral types earlier than L5 ($T_{\text{eff,L5}} \sim 1800$ K). Using the Sonora-Bobcat models, we estimate the temperature of LHS 1610 b at the lower bound of our age estimate (2.5 Gyr) and find a value of ~ 1100 K. Paired with the age estimate, LHS 1610 b seems unlikely to be the origin of the flares.

7.2. Stellar Wind Environment

For magnetic star-companion interactions to occur, the companion must orbit sub-Alfvénically, i.e., when the Alfvén Mach number (M_A) is less than 1 (see e.g., Saur et al. 2013, and references therein):

$$M_A = \Delta u / u_A < 1 \quad (17)$$

where Δu is the relative velocity of the stellar wind as seen by the orbiting planet and u_A is the Alfvén speed:

$$u_A = \frac{B_w}{\sqrt{4\pi\rho_w}}, \quad (18)$$

where B_w and ρ_w are the magnetic field strength and mass density of the stellar wind respectively.

To determine if LHS 1610 b is in a sub-Alfvénic orbit, we require knowledge of both the surface magnetic field and the wind of the star. Measurements of the winds of low-mass main sequence stars like LHS 1610 are both indirect and few in numbers. However, emerging trends relating the mass-loss rate per unit surface area to the surface X-ray fluxes of these stars can be used to estimate their wind properties (Vidotto 2021). Wood et al. (2021) presented the most up to date list of mass-loss rate estimates for low-mass main sequence stars. Including the estimate made for the F-type star HD 209458 by Kislyakova et al. (2014) for completeness, fitting the mass-loss rate per unit surface area \dot{M}/R_\star^2 to the surface X-ray flux F_X with a power law gives:

$$\log_{10} \left(\frac{\dot{M}}{R_\star^2} / \frac{\dot{M}_\odot}{R_\odot^2} \right) = (0.71 \pm 0.13) \log_{10} F_X - (3.09 \pm 0.69), \quad (19)$$

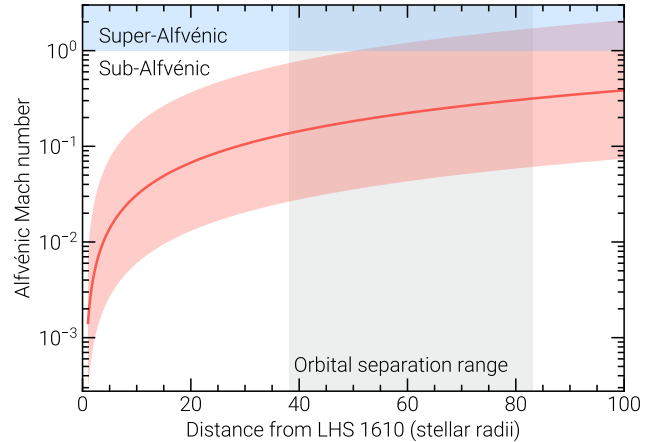


Figure 4. The Alfvén Mach number as a function of distance for LHS 1610. The solid red line shows the profile at the 50th percentile of our sampling method, and the shaded region shows the 16th to 84th %-ile region. The grey shaded region highlights the variations in orbital separation between LHS 1610 b and the host star. This changes significantly over the course of the orbit due to the eccentricity and mass ratio. The horizontal blue shaded region marks where the wind of the star becomes super-Alfvénic, in which the brown dwarf can no longer magnetically interact with the host star. This shows that in almost all cases that LHS 1610 b is on a sub-Alfvénic orbit, and capable of star-companion interactions.

where $\dot{M}_\odot = 2 \times 10^{-14} M_\odot \text{ yr}^{-1}$ is the mass-loss rate of the Sun (Cohen 2011) and F_X is reported in $\text{erg s}^{-1} \text{ cm}^{-2}$. Another key ingredient for estimating the wind properties of low-mass main sequence stars is their coronal temperature. Johnstone & Güdel (2015) found the following empirical relation between the observed surface X-ray flux and inferred coronal temperatures of these stars:

$$T = 0.11 F_X^{0.26} \times 10^6 \text{ K}. \quad (20)$$

To estimate where the wind of the host star becomes super-Alfvénic, we also must estimate the magnetic field strength at the stellar surface. The most relevant value in the context of stellar winds is $\langle B_V \rangle$, which is the unsigned average large-scale magnetic field strength. As the small-scale field strength drops off rapidly as a function of distance, its effects on the wind outflow are negligible (Jardine et al. 2017; Vidotto 2021). Kochukhov (2021) present a list of most $\langle B_V \rangle$ estimates for M dwarfs to date. Fitting their values of $\langle B_V \rangle$ as a function of the stellar rotation period P_{rot} , we find that:

$$\log_{10} \langle B_V \rangle = (-0.38 \pm 0.09) \log_{10} P_{\text{rot}} + (2.45 \pm 0.07), \quad (21)$$

where $\langle B_V \rangle$ is in Gauss and P_{rot} is in days.

To estimate the wind properties at the orbit of LHS 1610 b, we first choose 10,000 random sam-

ples for the X-ray luminosity, which is reported to be $10^{26.94 \pm 0.04}$ erg s $^{-1}$ (Magaudda et al. 2020), derived from X-ray observations with the *Chandra X-ray Observatory* (Weisskopf et al. 2000; Wright & Drake 2016; Wright et al. 2018). Converting these values to surface X-ray fluxes, we then estimate the mass-loss rate and coronal temperature of LHS 1610 via Equations 19 and 20. The resulting mass-loss rate and coronal temperature we derive for LHS 1610 are $\dot{M} = 10^{-1.19 \pm 1.39} \dot{M}_{\odot}$, and $T = (3.05 \pm 0.07) \times 10^6$ K, respectively. Similarly for the large-scale unsigned surface magnetic field strength, we randomly sample values for the rotation period of 84.3 ± 8 days, and estimate the field strength to be $\langle B_V \rangle = 10^{1.72 \pm 0.19}$ G using Equation 21.

Although LHS 1610 likely possesses a relatively strong surface magnetic field, its effects on the wind outflow are unlikely to be significant due to its slow rotation (Preusse et al. 2005; Johnstone 2017). It is therefore reasonable to assume that the acceleration of the stellar wind is driven predominantly by the thermal pressure gradient (Parker 1958). By doing so, we assume that the wind velocity and magnetic field are purely radial.

With the ranges of values for \dot{M} , T , and $\langle B_V \rangle$ estimated, we now use the code developed by Kavanagh & Vidotto (2020) to solve for the velocity profile of the stellar wind. Each value of T along with the stellar mass gives us the radial velocity of the wind $u_r(r)$ as a function of distance r , which we then use to estimate the density profile via the conservation of mass:

$$\rho_w(r) = \frac{\dot{M}}{4\pi u_r(r) r^2}. \quad (22)$$

The magnetic field strength as a function of distance can be obtained using the conservation of magnetic flux:

$$B_w(r) = \langle B_V \rangle \left(\frac{R_{\star}}{r} \right)^2. \quad (23)$$

We then compute the Alfvén velocity and Mach number as a function of distance using Equations 18 and 17 respectively for each set of values of \dot{M} , T , and $\langle B_V \rangle$. These are shown in Figure 4. We see that over the range of orbital distances of the companion, the vast majority of solutions place the companion in a sub-Alfvénic orbit entirely, satisfying the condition for sub-Alfvénic interactions occurring with the large-scale magnetic field of the host star.

7.3. Sub-Alfvénic interactions between LHS 1610 b and its host star

If LHS 1610 b is in a sub-Alfvénic orbit, it could enhance emission on the host star at a wide range of wavelengths by the dissipation of energy carried by Alfvén

waves generated via sub-Alfvénic interactions (Zarka 2007; Saur et al. 2013). The power produced via these interactions is (Saur et al. 2013; Kavanagh et al. 2022):

$$P_{\text{SA}} = \pi^{1/2} R_{\text{obs}}^2 B_w \rho_w^{1/2} \Delta u^2 \sin^2 \theta, \quad (24)$$

where R_{obs} is the size the obstacle perturbing the stellar magnetic field, and θ is the angle between the relative velocity and magnetic field vectors $\Delta \vec{u}$ and \vec{B}_w . In the case that LHS 1610 b is unmagnetised, R_{obs} is simply its radius R_{BD} . However, if it possesses an intrinsic magnetic field, the size of the obstacle is the size of its magnetopause R_{M} , the point where the pressure of the incident stellar wind balances with the pressure exerted by the magnetic field of LHS 1610 b (Vidotto et al. 2012):

$$R_{\text{M}} = \left(\frac{B_{\text{BD}}^2}{32\pi p_w} \right)^{1/6} R_{\text{BD}}. \quad (25)$$

Here B_{BD} is the field strength of LHS 1610 b at its magnetic poles, assuming the field is dipolar, and p_w is the pressure of the stellar wind at its orbit:

$$p_w = \rho_w (a^2 + \Delta u^2) + \frac{B_w^2}{8\pi}, \quad (26)$$

where $a = \sqrt{2kT/m_p}$ is the isothermal sound speed.

Due to no published radio emission detection from LHS 1610 b, we cannot determine its magnetic field strength directly. Therefore, we use the following theoretical prescription for the magnetic field strengths of sub-stellar objects derived by Reiners & Christensen (2010) to estimate the polar magnetic field strength of LHS 1610 b:

$$B_{\text{BD}} = 3.39 \left(\frac{M_{\text{BD}} L_{\text{BD}}^2}{R_{\text{BD}}^7} \right)^{1/6} \text{ kG}. \quad (27)$$

The luminosity L_{BD} and radius R_{BD} of the brown dwarf can be estimated from isochrones if its mass and age are known. However, the uncertainty on the age of the system is large. Therefore, we consider ages of 2, 7, and 12 Gyr for LHS 1610 b. Using the solar metallicity isochrones provided by Marley et al. (2021), at these ages we estimate radii for LHS 1610 b of 0.86, 0.80, and 0.78 R_{Jup} respectively. Note that propagating the error in mass here results in errors less than 0.01 R_{Jup} . Following the same procedure for the luminosity, we estimate the field strength for LHS 1610 b at the ages of 2, 7, and 12 Gyr via Equation 27: 849 ± 20 , 515 ± 12 , and 418 ± 10 G. The corresponding magnetopause sizes LHS 1610 b at these ages are large, varying from from around 12 to 35 Jupiter radii depending on the wind conditions and orbital phase.

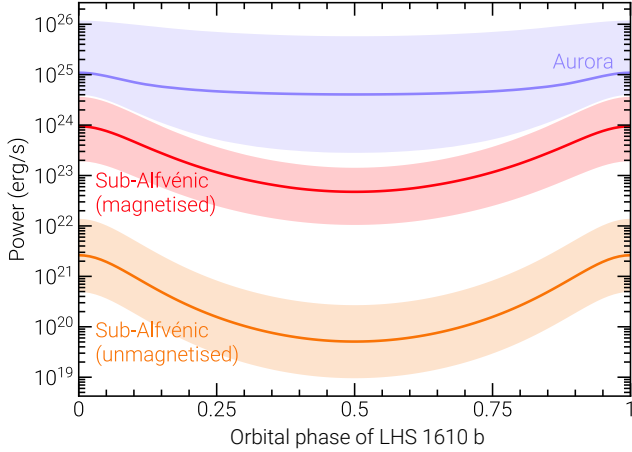


Figure 5. Estimated powers from both sub-Alfvénic interactions between LHS 1610 b (red and orange curves) and its host star and wind-magnetospheric interactions between the wind of the host star and the brown dwarf’s magnetosphere (purple curves). Each solid line and shaded region shows the median and the 1σ region, respectively. The powers are shown as a function of orbital phase, which are modulated due to the eccentricity of the orbit. For the sub-Alfvénic powers, cases are shown where the brown dwarf is both magnetised (red curves) and unmagnetised (orange curves). The results here are shown for an age of 7 Gyr for the brown dwarf. In all cases, a fraction of the energy ($10^{-4} - 10^{-2}$) is expected to be released at radio wavelengths, resulting in flux estimates that are within reach of sensitive radio telescopes such as LOFAR.

With both the estimates for the properties of the stellar wind and the obstacle size of the brown dwarf established, we now use Equation 26 to estimate the power dissipated along the stellar magnetic field via sub-Alfvénic interactions. We consider the cases where LHS 1610 b is both magnetised and weakly/unmagnetised (i.e., $R_{\text{obs}} \approx R_{\text{BD}}$ in Equation 26).

In Figure 5 we show the estimated power generated via sub-Alfvénic interactions between the brown dwarf and stellar magnetic field as a function of orbital phase, for an age of 7 Gyr. For the magnetised case, we estimate the total power produced to be within the range of $\sim 10^{22}$ to 10^{24} erg s^{-1} , whereas in the unmagnetised case, it ranges from $\sim 10^{19}$ to 10^{22} erg s^{-1} . Due to the eccentricity of the orbit, the distance between the two bodies varies from 38 to 83 R_{\star} over the course of the orbit. As a result, the brown dwarf is subjected to time-varying stellar wind conditions. Therefore, the power dissipated onto the star also varies, as is seen in the lightcurves in Figure 5. Note that differences in the power are less than 60% for ages of 2 Gyr and 12 Gyr,

irrespective of whether the brown dwarf is magnetised or not.

If the estimated power generated by sub-Alfvénic interactions P_{SA} is indeed dissipated onto the star’s magnetic field, some fraction is expected to manifest as bright radio emission via the electron cyclotron maser (ECM) instability (Zarka 2007; Saur et al. 2013). For the Io-induced emission on Jupiter, this fraction or ‘efficiency ratio’ is estimated to be around 10^{-4} to 10^{-2} (Turnpenney et al. 2018; Saur et al. 2021). If we assume this fraction of the total power P_{radio} is uniformly dissipated in the radio over the frequency range $\Delta\nu$, the flux density observed at a distance d is:

$$F_{\nu} = \frac{P_{\text{radio}}}{d^2 \Omega_{\text{beam}} \Delta\nu}, \quad (28)$$

where Ω_{beam} is the solid angle of the emission beam, which is a hollow cone since ECM emission is beamed. Typical values assumed for Ω range from 0.16 to 1.6 steradian (Zarka et al. 2004; Turnpenney et al. 2018). If the frequency range $\Delta\nu$ is sufficiently wide, it is effectively equal to the cutoff frequency ν_{max} , which we assume to be that at the stellar surface. Given that ECM emission occurs at the local cyclotron frequency (Dulk 1985), the cutoff frequency is therefore the cyclotron frequency at the surface:

$$\nu_{\text{max}} = 2.8 \langle B_V \rangle \text{ MHz}, \quad (29)$$

where $\langle B_V \rangle$ is the unsigned surface average field strength in Gauss.

Let’s consider a conservative scenario, in which $P_{\text{radio}} = 10^{-5} P_{\text{SA}}$ and $\Omega = 1.6$ sr. For the unmagnetised and magnetised cases, the sub-Alfvénic radio fluxes produced range from $\sim 2 \times 10^{-3}$ to 2 mJy and ~ 2 to 200 mJy respectively. The corresponding frequency range is around 100 to 230 MHz based on the estimated surface field strength. Emission in this range at a mJy level is well within the capabilities for detection with radio telescopes such as LOFAR and GMRT (see Narang et al. 2021; Callingham et al. 2021). Therefore, LHS 1610 is a compelling case for follow-up searches in the radio for signatures of star-companion interactions.

We note also that since ECM emission is beamed, the visibility of the radio emission is highly dependent on the underlying system geometry (Kavanagh & Vedantham 2023). By combining the orbital characteristics derived in this work with efforts to map the surface magnetic field topology via Zeeman Doppler imaging (e.g. Klein et al. 2021), we could estimate at what orbital phases we would expect to see the radio emission. In addition to potential radio emission, signatures of star-companion interactions occurring in the system may be visible at

different wavelengths such as in the optical (see Section 7.1), UV, and infrared (Shkolnik et al. 2005; Klein et al. 2022).

7.4. Auroral emission from LHS 1610 b

Regardless of whether LHS 1610 b is in a sub-Alfvénic orbit or not, if it possesses an intrinsic magnetic field, it may also exhibit strong auroral emission produced via the dissipation of the energy carried by the stellar wind onto its magnetosphere (Zarka 2007). For the magnetised bodies in the solar system, their observed auroral emission at radio wavelengths scales linearly with the solar wind power intercepted by their magnetospheres. The power intercepted is (Zarka 2007):

$$P_{\text{aurora}} = \varepsilon \Delta u \pi R_M^2, \quad (30)$$

where $\varepsilon = \varepsilon_{\text{kin}} + \varepsilon_{\text{mag}} + \varepsilon_{\text{th}}$ is the energy density of the incident wind, which is comprised of a kinetic, magnetic, and thermal component:

$$\varepsilon_{\text{kin}} = \rho_w \Delta u^2, \quad (31)$$

$$\varepsilon_{\text{mag}} = \frac{B_w^2 \sin^2 \theta}{4\pi}, \quad (32)$$

$$\varepsilon_{\text{th}} = a^2 \rho. \quad (33)$$

In the solar system, generally only the kinetic and thermal components are considered, which both appear to produce powers that are directly proportional to the observed auroral radio power, with around 10^{-5} to 10^{-3} of the incident power being dissipated (Zarka 2007). For completeness, we also included the thermal energy incident on the magnetosphere (Elekes & Saur 2023). In a similar manner to Section 7.3, we compute the incident power on the magnetosphere of LHS 1610 b as a function of its orbital phase, considering the uncertainties in the wind properties. This is shown in Figure 5 alongside the powers estimated in Section 7.3 from sub-Alfvénic interactions. We again find large powers between $\sim 10^{23}$ to $\sim 10^{26}$ erg s $^{-1}$ thanks to the large size of its magnetopause, which varies from around 15 to 35 Jupiter radii over the course of its orbit.

We now compute the radio flux via Equation 28, again choosing conservative values for $\Omega = 1.6$ sr and the efficiency ratio of 10^{-6} , which is an order of magnitude lower than the minimum value estimated for auroral radio emission in the solar system. We set the cyclotron frequency at the magnetic poles of the brown dwarf as the cutoff frequency as the field lines on which the aurora is driven likely connect back close to the magnetic poles due to the large size of the magnetopause. At an age of 7 Gyr, this frequency is ~ 1.4 GHz. We find that with these estimates, the flux density should

range from 0.2 to 200 mJy. At GHz frequencies, the VLA would be suitable for follow-up observations (e.g., Villadsen & Hallinan 2019). This highlights the benefit of carrying out a multiwavelength radio campaign of the system, in that we could determine if sub-Alfvénic interactions and/or aurorae could be detected by observing at both MHz and GHz frequencies. Such observations could constrain both the sub/super-Alfvénic nature of the companion, and also the field strengths of both objects. Again, the visibility of this emission is dependent on the geometry of the brown dwarf’s magnetic field, which is unknown. Auroral emission is also a possibility at other wavelengths. If the brown dwarf was isolated, its auroral emission would be the most favourable for detection at UV wavelengths (Saur et al. 2021).

8. SUMMARY

We studied the LHS 1610 system, a nearby M5 dwarf ($d = 9.7$ pc) hosting a brown dwarf in a short period $P = 10.6$ day eccentric ($e = 0.37$) orbit. This system is the second closest M dwarf with a substellar companion and a Gaia two-body solution behind GJ 876, an M dwarf system hosting at least four known planets.

Jointly modeling the available RVs from HPF and TRES with the Gaia two-body solution, we are able to determine all of the orbital elements of LHS 1610 b. We obtain an orbital inclination of $i_* = 117.2 \pm 0.9^\circ$, resulting in a mass constraint of $M = 50.9 \pm 0.9 M_J$, confirming the brown dwarf nature of the companion. We highlight the discrepancy between the RV-only fit eccentricity ($e = 0.37$) and that of the Gaia two-body solution ($e = 0.52$). This discrepancy may impact the result of the joint fit, and we note the necessity to revisit this when the astrometric data are released in Gaia DR4.

We find that LHS 1610 b is the second most precisely known brown dwarf mass within 25 parsecs behind GJ 229 B, which is potentially an unresolved binary. It is also the most eccentric brown dwarf orbiting an M dwarf behind GJ 229 B.

Due to LHS 1610 b’s large radius and close-in orbit around a nearby mid M star, LHS 1610 b is a promising target for the detection of potential sub-Alfvénic star-companion interactions at a wide range of wavelengths. Using the available TESS data, we derive a flare rate of 0.28 ± 0.7 flares/day. When accounting for a flare energy cut-off ($E > 10^{31.5}$), the subsequent flare rate places LHS 1610 among the high end for its rotation period amongst a volume-complete sample of mid-to-late M stars within 15 pc from Medina et al. (2020) and Medina et al. (2022). Within this sample, LHS 1610 is similar in spectral type, flare rate, and rotation period to Proxima Centauri and YZ Ceti, both of which have observed ra-

dio emission attributed to possible star-companion interactions. Using the available TESS data for LHS 1610, we detected no significant phase-dependence of the flares, and highlight that additional data would be needed to decisively confirm or rule out such a dependence.

We simulated the expected energetics of both sub-Alfvénic interactions and direct auroral emission from the brown dwarf. For the star-companion interactions, we demonstrate that LHS 1610 b likely resides in a sub-Alfvénic orbit over its variable range of orbital distances due to its eccentricity, a necessary requirement to support star-companion interactions. We show that given even conservative estimates, the radio emission expected from the star due to these interactions is within the sensitivity range of LOFAR. Additionally, we show that direct auroral emission from the brown dwarf could be even more easily detectable than the radio emission from star-planet interactions, with nominal expected radio powers in the $10^{24} - 10^{26}$ erg/s range. The detection of either of these interactions is dependent on the orbital phase of the brown dwarf, which benefit from the full orbital solution and precise ephemeris provided in Table 2.

Facilities: HPF/HET 10m, TRES, TESS, *Gaia*.

Software: `astropy` (Astropy Collaboration et al. 2013), `barycorrpy` (Kanodia & Wright 2018), `corner.py` (Foreman-Mackey 2016), `emcee` (Foreman-Mackey et al. 2013), `Jupyter` (Kluyver et al. 2016), `matplotlib` (Hunter 2007), `numpy` (Van Der Walt et al. 2011), `pandas` (McKinney 2010), `pyde` (Parviainen 2016), `radvel` (Fulton et al. 2018), `SERVAL` (Zechmeister et al. 2018), `HxRGproc` (Ninan et al. 2018).

Acknowledgements: GS acknowledges support provided by NASA through the NASA Hubble Fellowship grant HST-HF2-51519.001-A awarded by the Space Telescope Science Institute, which is operated by the Association of Universities for Research in Astronomy, Inc., for NASA, under contract NAS5-26555. RDK acknowledges funding from the Dutch Research Council (NWO) for the e-MAPS (exploring magnetism on the planetary scale) project (project number VI.Vidi.203.093) under the NWO talent scheme Vidi.

This work was partially supported by funding from the Center for Exoplanets and Habitable Worlds. The Center for Exoplanets and Habitable Worlds is supported by the Pennsylvania State University, the Eberly College of Science, and the Pennsylvania Space Grant Consortium. CIC acknowledges support by NASA Headquarters through an appointment to the NASA Postdoctoral Program at the Goddard Space Flight Center, administered by URSA through a contract with NASA. This work was performed for the Jet Propulsion Laboratory, California Institute of Technology, sponsored by the United States Government under the Prime Contract 80NM0018D0004 between Caltech and NASA. We acknowledge support from NSF grant AST-1909506, AST-190950, AST-1910954, AST-1907622. Computations for this research were performed on the Pennsylvania State University’s Institute for Computational & Data Sciences (ICDS).

These results are based on observations obtained with the Habitable-zone Planet Finder Spectrograph on the HET. We acknowledge support from NSF grants AST 1006676, AST 1126413, AST 1310875, AST 1310885, and the NASA Astrobiology Institute (NNA09DA76A) in our pursuit of precision radial velocities in the NIR. We acknowledge support from the Heising-Simons Foundation via grant 2017-0494. This research was conducted in part under NSF grants AST-2108493, AST-2108512, AST-2108569, and AST-2108801 in support of the HPF Guaranteed Time Observations survey. The Hobby-Eberly Telescope is a joint project of the University of Texas at Austin, the Pennsylvania State University, Ludwig-Maximilians-Universität München, and Georg-August Universität Göttingen. The HET is named in honor of its principal benefactors, William P. Hobby and Robert E. Eberly. The HET collaboration acknowledges the support and resources from the Texas Advanced Computing Center. We thank the Resident astronomers and Telescope Operators at the HET for the skillful execution of our observations with HPF.

BJSP acknowledges and pays respect to the traditional owners of the land on which the University of Queensland is situated, and to their Ancestors and de-

scendants, who continue cultural and spiritual connections to Country.

This research has made use of data obtained from or tools provided by the portal exoplanet.eu of The Extrasolar Planets Encyclopaedia.

This work has made use of data from the European Space Agency (ESA) mission *Gaia* (<https://www.cosmos.esa.int/gaia>), processed by the *Gaia* Data Processing and Analysis Consortium (DPAC, <https://www.cosmos.esa.int/web/gaia/dpac/consortium>). Funding for the DPAC has been provided by national institutions, in particular the institutions participating in the *Gaia* Multilateral Agreement.

This research made use of Astropy, a community-developed core Python package for Astronomy ([Astropy Collaboration et al. 2013](#)).

APPENDIX

A. TESS FLARES

We show the TESS photometry in Figure 6 and highlight the flares identified from our analysis using the `stella` (Feinstein et al. 2020a) flare-finding algorithm. The flares are highlighted by vertical grey bars. Points are color coded by the flare probability assigned by `stella`, where red points have a probability greater than 0.6, and grey points are those below 0.6. We show the individual TESS Sectors 42, 43, and 44 in panels A, B, and C, respectively. Panel D shows the combined data from all sectors, phase folded on the orbital period and centered at the periastron time. As highlighted in Section 7.1, we don't see evidence for phase-dependence of the flares.

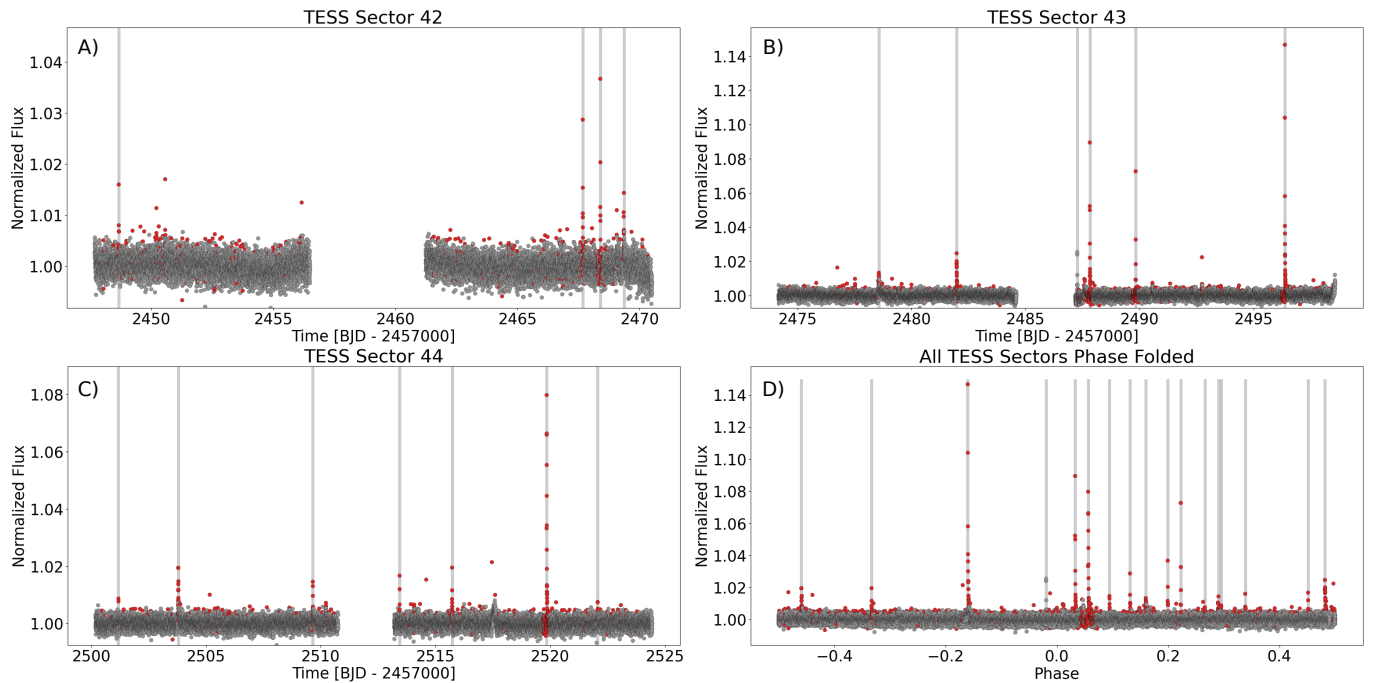


Figure 6. Flares in TESS Photometry: Panels **A**, **B**, and **C** show individual sector light curves for TESS Sectors 42, 43, and 44 respectively. Points are colored by flare probability assigned by `stella`: Red show a probability $> 60\%$, and grey points less than a probability of $< 60\%$. Flares that passed our cuts are highlighted by the vertical grey bars. Panel **D** contains the combination of all sectors phase folded on the period centered on the time of periastron. Flares are again highlighted by vertical grey bars. We do not see statistically significant evidence for phase-dependent flaring.

B. RADIAL VELOCITIES

Table 3. Radial Velocities for LHS 1610A

BJD (days)	RV (km s ⁻¹)	RV error (km s ⁻¹)	Instrument
2457785.7131	28.448	0.028	TRES
2457786.7850	32.365	0.028	TRES
2457787.6378	35.502	0.028	TRES
2457794.6483	22.514	0.028	TRES
2457795.7182	26.224	0.028	TRES
2457800.7416	44.533	0.028	TRES
2457806.6698	27.585	0.028	TRES
2457807.6875	31.293	0.029	TRES
2457808.6590	34.944	0.028	TRES
2457821.6194	43.586	0.028	TRES
2457822.6458	45.893	0.029	TRES
2457823.6552	40.479	0.031	TRES
2457824.6210	25.451	0.029	TRES
2459092.921787	-0.9804	0.0036	HPF
2459157.934541	1.1535	0.0028	HPF
2459185.659386	-10.612	0.003	HPF
2459212.786561	-21.375	0.006	HPF
2459274.599746	0.6958	0.0061	HPF
2459621.664956	-4.5927	0.0092	HPF

TRES RVs are adopted as provided in [Winters et al. \(2018\)](#).

C. JOINT FIT POSTERiors

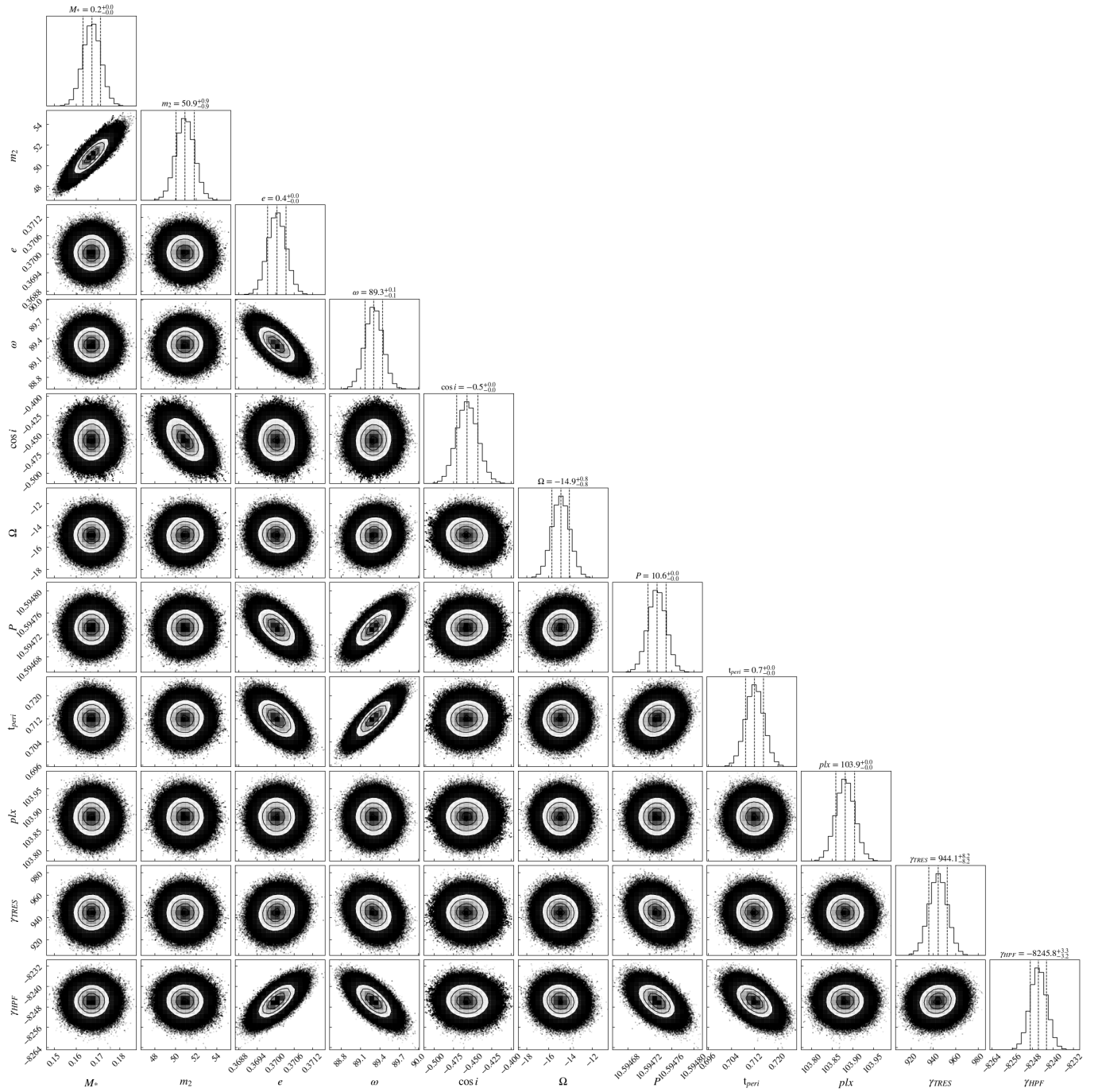


Figure 7. Corner plot showing the posterior distributions of the joint Gaia and RV fit from Section 4.3. Median values are highlighted in Table 2.

REFERENCES

- Akeson, R. L., Chen, X., Ciardi, D., et al. 2013, *PASP*, 125, 989, doi: [10.1086/672273](https://doi.org/10.1086/672273)
- Anglada-Escudé, G., Amado, P. J., Barnes, J., et al. 2016, *Nature*, 536, 437, doi: [10.1038/nature19106](https://doi.org/10.1038/nature19106)
- Astropy Collaboration, Robitaille, T. P., Tollerud, E. J., et al. 2013, *A&A*, 558, A33, doi: [10.1051/0004-6361/201322068](https://doi.org/10.1051/0004-6361/201322068)
- Bailer-Jones, C. A. L., Rybizki, J., Fouesneau, M., Mantelet, G., & Andrae, R. 2018, *AJ*, 156, 58, doi: [10.3847/1538-3881/aacb21](https://doi.org/10.3847/1538-3881/aacb21)
- Blanco-Pozo, J., Perger, M., Damasso, M., et al. 2023, *A&A*, 671, A50, doi: [10.1051/0004-6361/202245053](https://doi.org/10.1051/0004-6361/202245053)
- Bonomo, A. S., Desidera, S., Benatti, S., et al. 2017, *A&A*, 602, A107, doi: [10.1051/0004-6361/201629882](https://doi.org/10.1051/0004-6361/201629882)
- Bowler, B. P., Blunt, S. C., & Nielsen, E. L. 2020, *AJ*, 159, 63, doi: [10.3847/1538-3881/ab5b11](https://doi.org/10.3847/1538-3881/ab5b11)
- Brandt, G. M., Dupuy, T. J., Li, Y., et al. 2021, *AJ*, 162, 301, doi: [10.3847/1538-3881/ac273e](https://doi.org/10.3847/1538-3881/ac273e)
- Buchhave, L. A., Bakos, G. Á., Hartman, J. D., et al. 2010, *ApJ*, 720, 1118, doi: [10.1088/0004-637X/720/2/1118](https://doi.org/10.1088/0004-637X/720/2/1118)
- Burn, R., Schlecker, M., Mordasini, C., et al. 2021, *A&A*, 656, A72, doi: [10.1051/0004-6361/202140390](https://doi.org/10.1051/0004-6361/202140390)
- Cañas, C. I., Mahadevan, S., Bender, C. F., et al. 2022, *AJ*, 163, 89, doi: [10.3847/1538-3881/ac415f](https://doi.org/10.3847/1538-3881/ac415f)
- Callingham, J. R., Vedantham, H. K., Shimwell, T. W., et al. 2021, *Nature Astronomy*, 5, 1233, doi: [10.1038/s41550-021-01483-0](https://doi.org/10.1038/s41550-021-01483-0)
- Chabrier, G., Johansen, A., Janson, M., & Rafikov, R. 2014, in *Protostars and Planets VI*, ed. H. Beuther, R. S. Klessen, C. P. Dullemond, & T. Henning, 619–642, doi: [10.2458/azu_uapress_9780816531240-ch027](https://doi.org/10.2458/azu_uapress_9780816531240-ch027)
- Choi, J., Dotter, A., Conroy, C., et al. 2016, *ApJ*, 823, 102, doi: [10.3847/0004-637X/823/2/102](https://doi.org/10.3847/0004-637X/823/2/102)
- Cohen, O. 2011, *MNRAS*, 417, 2592, doi: [10.1111/j.1365-2966.2011.19428.x](https://doi.org/10.1111/j.1365-2966.2011.19428.x)
- Currie, T., Brandt, G. M., Brandt, T. D., et al. 2023, *Science*, 380, 198, doi: [10.1126/science.abo6192](https://doi.org/10.1126/science.abo6192)
- Damiani, C., & Díaz, R. F. 2016, *A&A*, 589, A55, doi: [10.1051/0004-6361/201527100](https://doi.org/10.1051/0004-6361/201527100)
- Dotter, A. 2016, *ApJS*, 222, 8, doi: [10.3847/0067-0049/222/1/8](https://doi.org/10.3847/0067-0049/222/1/8)
- Dulk, G. A. 1985, *ARA&A*, 23, 169, doi: [10.1146/annurev.aa.23.090185.001125](https://doi.org/10.1146/annurev.aa.23.090185.001125)
- Dupuy, T. J., Liu, M. C., Best, W. M. J., et al. 2019, *AJ*, 158, 174, doi: [10.3847/1538-3881/ab3cd1](https://doi.org/10.3847/1538-3881/ab3cd1)
- Duquennoy, A., & Mayor, M. 1991, *A&A*, 248, 485
- Eastman, J. D., Rodriguez, J. E., Agol, E., et al. 2019, arXiv e-prints, arXiv:1907.09480, doi: [10.48550/arXiv.1907.09480](https://doi.org/10.48550/arXiv.1907.09480)
- Elekes, F., & Saur, J. 2023, *A&A*, 671, A133, doi: [10.1051/0004-6361/202244947](https://doi.org/10.1051/0004-6361/202244947)
- Faria, J. P., Suárez Mascareño, A., Figueira, P., et al. 2022, *A&A*, 658, A115, doi: [10.1051/0004-6361/202142337](https://doi.org/10.1051/0004-6361/202142337)
- Feinstein, A., Montet, B., & Ansdell, M. 2020a, *The Journal of Open Source Software*, 5, 2347, doi: [10.21105/joss.02347](https://doi.org/10.21105/joss.02347)
- Feinstein, A. D., Montet, B. T., Ansdell, M., et al. 2020b, *AJ*, 160, 219, doi: [10.3847/1538-3881/abac0a](https://doi.org/10.3847/1538-3881/abac0a)
- Foreman-Mackey, D. 2016, *JOSS*, 24, doi: [10.21105/joss.00024](https://doi.org/10.21105/joss.00024)
- Foreman-Mackey, D., Hogg, D. W., Lang, D., & Goodman, J. 2013, *PASP*, 125, 306, doi: [10.1086/670067](https://doi.org/10.1086/670067)
- Fulton, B. J., Petigura, E. A., Blunt, S., & Sinukoff, E. 2018, *PASP*, 130, 044504, doi: [10.1088/1538-3873/aaaaa8](https://doi.org/10.1088/1538-3873/aaaaa8)
- Gaia Collaboration, Prusti, T., de Bruijne, J. H. J., et al. 2016, *A&A*, 595, A1, doi: [10.1051/0004-6361/201629272](https://doi.org/10.1051/0004-6361/201629272)
- Gaia Collaboration, Arenou, F., Babusiaux, C., et al. 2022, arXiv e-prints, arXiv:2206.05595, doi: [10.48550/arXiv.2206.05595](https://doi.org/10.48550/arXiv.2206.05595)
- Gaia Collaboration, Vallenari, A., Brown, A. G. A., et al. 2023, *A&A*, 674, A1, doi: [10.1051/0004-6361/202243940](https://doi.org/10.1051/0004-6361/202243940)
- Gallet, F., Bolmont, E., Mathis, S., Charbonnel, C., & Amard, L. 2017, *A&A*, 604, A112, doi: [10.1051/0004-6361/201730661](https://doi.org/10.1051/0004-6361/201730661)
- Gizis, J. E., Paudel, R. R., Mullan, D., et al. 2017, *ApJ*, 845, 33, doi: [10.3847/1538-4357/aa7da0](https://doi.org/10.3847/1538-4357/aa7da0)
- Goldreich, P., & Soter, S. 1966, *Icarus*, 5, 375, doi: [10.1016/0019-1035\(66\)90051-0](https://doi.org/10.1016/0019-1035(66)90051-0)
- Guillot, T., Burrows, A., Hubbard, W. B., Lunine, J. I., & Saumon, D. 1996, *ApJL*, 459, L35, doi: [10.1086/309935](https://doi.org/10.1086/309935)
- Halbwachs, J. L., Mayor, M., & Udry, S. 2005, *A&A*, 431, 1129, doi: [10.1051/0004-6361:20041219](https://doi.org/10.1051/0004-6361:20041219)
- Halbwachs, J.-L., Pourbaix, D., Arenou, F., et al. 2023, *A&A*, 674, A9, doi: [10.1051/0004-6361/202243969](https://doi.org/10.1051/0004-6361/202243969)
- Hogg, D. W., & Foreman-Mackey, D. 2018, *ApJS*, 236, 11, doi: [10.3847/1538-4365/aab76e](https://doi.org/10.3847/1538-4365/aab76e)
- Holl, B., Sozzetti, A., Sahlmann, J., et al. 2022, arXiv e-prints, arXiv:2206.05439, doi: [10.48550/arXiv.2206.05439](https://doi.org/10.48550/arXiv.2206.05439)
- Howe, A. R., Mandell, A. M., & McElwain, M. W. 2023, arXiv e-prints, arXiv:2306.08450, doi: [10.48550/arXiv.2306.08450](https://doi.org/10.48550/arXiv.2306.08450)
- Hunter, J. D. 2007, *Computing in Science and Engineering*, 9, 90, doi: [10.1109/MCSE.2007.55](https://doi.org/10.1109/MCSE.2007.55)
- Husser, T. O., Wende-von Berg, S., Dreizler, S., et al. 2013, *A&A*, 553, A6, doi: [10.1051/0004-6361/201219058](https://doi.org/10.1051/0004-6361/201219058)
- Ilin, E., & Poppenhaeger, K. 2022, *MNRAS*, 513, 4579, doi: [10.1093/mnras/stac1232](https://doi.org/10.1093/mnras/stac1232)

- Irwin, J. M., Berta-Thompson, Z. K., Charbonneau, D., et al. 2015, in *Cambridge Workshop on Cool Stars, Stellar Systems, and the Sun*, Vol. 18, 18th Cambridge Workshop on Cool Stars, Stellar Systems, and the Sun, 767–772, doi: [10.48550/arXiv.1409.0891](https://doi.org/10.48550/arXiv.1409.0891)
- Jackson, B., Greenberg, R., & Barnes, R. 2008, *ApJ*, 678, 1396, doi: [10.1086/529187](https://doi.org/10.1086/529187)
- Jardine, M., Vidotto, A. A., & See, V. 2017, *MNRAS*, 465, L25, doi: [10.1093/mnrasl/slw206](https://doi.org/10.1093/mnrasl/slw206)
- Johnstone, C. P. 2017, *A&A*, 598, A24, doi: [10.1051/0004-6361/201629609](https://doi.org/10.1051/0004-6361/201629609)
- Johnstone, C. P., & Güdel, M. 2015, *A&A*, 578, A129, doi: [10.1051/0004-6361/201425283](https://doi.org/10.1051/0004-6361/201425283)
- Kanodia, S., & Wright, J. 2018, *RNAAS*, 2, 4, doi: [10.3847/2515-5172/aaa4b7](https://doi.org/10.3847/2515-5172/aaa4b7)
- Kavanagh, R. D., & Vedantham, H. K. 2023, *MNRAS*, 524, 6267, doi: [10.1093/mnras/stad2035](https://doi.org/10.1093/mnras/stad2035)
- Kavanagh, R. D., & Vidotto, A. A. 2020, *MNRAS*, 493, 1492, doi: [10.1093/mnras/staa422](https://doi.org/10.1093/mnras/staa422)
- Kavanagh, R. D., Vidotto, A. A., Vedantham, H. K., et al. 2022, *MNRAS*, 514, 675, doi: [10.1093/mnras/stac1264](https://doi.org/10.1093/mnras/stac1264)
- Kislyakova, K. G., Holmström, M., Lammer, H., Odert, P., & Khodachenko, M. L. 2014, *Science*, 346, 981, doi: [10.1126/science.1257829](https://doi.org/10.1126/science.1257829)
- Klein, B., Donati, J.-F., Hébrard, É. M., et al. 2021, *MNRAS*, 500, 1844, doi: [10.1093/mnras/staa3396](https://doi.org/10.1093/mnras/staa3396)
- Klein, B., Zicher, N., Kavanagh, R. D., et al. 2022, *MNRAS*, 512, 5067, doi: [10.1093/mnras/stac761](https://doi.org/10.1093/mnras/stac761)
- Kluyver, T., Ragan-Kelley, B., Pérez, F., et al. 2016, in *Positioning and Power in Academic Publishing: Players, Agents and Agendas*, ed. F. Loizides & B. Schmidt (IOS Press), 87–90. <https://eprints.soton.ac.uk/403913/>
- Kochukhov, O. 2021, *A&A Rv*, 29, 1, doi: [10.1007/s00159-020-00130-3](https://doi.org/10.1007/s00159-020-00130-3)
- Lainey, V. 2016, *Celestial Mechanics and Dynamical Astronomy*, 126, 145, doi: [10.1007/s10569-016-9695-y](https://doi.org/10.1007/s10569-016-9695-y)
- Lainey, V., Arlot, J., Karatekin, O., & Van Hoolst, T. 2009, in *AAS/Division for Planetary Sciences Meeting Abstracts*, Vol. 41, AAS/Division for Planetary Sciences Meeting Abstracts #41, 66.01
- Lanza, A. F. 2018, *A&A*, 610, A81, doi: [10.1051/0004-6361/201731414](https://doi.org/10.1051/0004-6361/201731414)
- Lattanzi, M. G., Spagna, A., Sozzetti, A., & Casertano, S. 2000, *MNRAS*, 317, 211, doi: [10.1046/j.1365-8711.2000.03637.x](https://doi.org/10.1046/j.1365-8711.2000.03637.x)
- Li, Y., Brandt, T. D., Brandt, G. M., et al. 2023, *MNRAS*, 522, 5622, doi: [10.1093/mnras/stad1315](https://doi.org/10.1093/mnras/stad1315)
- Lightkurve Collaboration, Cardoso, J. V. d. M., Hedges, C., et al. 2018, *Lightkurve: Kepler and TESS time series analysis in Python*, ASCL. <http://ascl.net/1812.013>
- Ma, B., & Ge, J. 2014, *MNRAS*, 439, 2781, doi: [10.1093/mnras/stu134](https://doi.org/10.1093/mnras/stu134)
- Magaudda, E., Stelzer, B., Covey, K. R., et al. 2020, *A&A*, 638, A20, doi: [10.1051/0004-6361/201937408](https://doi.org/10.1051/0004-6361/201937408)
- Mahadevan, S., Ramsey, L., Bender, C., et al. 2012, in *Proc. SPIE*, Vol. 8446, , 84461S, doi: [10.1117/12.926102](https://doi.org/10.1117/12.926102)
- Mahadevan, S., Ramsey, L. W., Terrien, R., et al. 2014, in *Proc. SPIE*, Vol. 9147, , 91471G, doi: [10.1117/12.2056417](https://doi.org/10.1117/12.2056417)
- Mann, A. W., Feiden, G. A., Gaidos, E., Boyajian, T., & von Braun, K. 2015, *ApJ*, 804, 64, doi: [10.1088/0004-637X/804/1/64](https://doi.org/10.1088/0004-637X/804/1/64)
- Mann, A. W., Dupuy, T., Kraus, A. L., et al. 2019, *Astrophysical Journal*, 871, 63, doi: [10.3847/1538-4357/aaf3bc](https://doi.org/10.3847/1538-4357/aaf3bc)
- Marcussen, M. L., & Albrecht, S. H. 2023, *AJ*, 165, 266, doi: [10.3847/1538-3881/acd53d](https://doi.org/10.3847/1538-3881/acd53d)
- Marley, M. S., Saumon, D., Visscher, C., et al. 2021, *ApJ*, 920, 85, doi: [10.3847/1538-4357/ac141d](https://doi.org/10.3847/1538-4357/ac141d)
- Mayor, M., Udry, S., Halbwachs, J. L., & Arenou, F. 2001, in *The Formation of Binary Stars*, ed. H. Zinnecker & R. Mathieu, Vol. 200, 45
- Mazeh, T. 2008, in *EAS Publications Series*, Vol. 29, *EAS Publications Series*, ed. M. J. Goupil & J. P. Zahn, 1–65, doi: [10.1051/eas:0829001](https://doi.org/10.1051/eas:0829001)
- McKinney, W. 2010, in *Proceedings of the 9th Python in Science Conference*, ed. S. van der Walt & J. Millman, 51 – 56
- Medina, A. A., Winters, J. G., Irwin, J. M., & Charbonneau, D. 2020, *ApJ*, 905, 107, doi: [10.3847/1538-4357/abc686](https://doi.org/10.3847/1538-4357/abc686)
- . 2022, *ApJ*, 935, 104, doi: [10.3847/1538-4357/ac77f9](https://doi.org/10.3847/1538-4357/ac77f9)
- Meibom, S., & Mathieu, R. D. 2005, in *Astronomical Society of the Pacific Conference Series*, Vol. 333, *Tidal Evolution and Oscillations in Binary Stars*, ed. A. Claret, A. Giménez, & J. P. Zahn, 95
- Metcalf, A. J., Anderson, T., Bender, C. F., et al. 2019, *Optica*, 6, 233, doi: [10.1364/OPTICA.6.000233](https://doi.org/10.1364/OPTICA.6.000233)
- Miguel, Y., Cridland, A., Ormel, C. W., Fortney, J. J., & Ida, S. 2020, *MNRAS*, 491, 1998, doi: [10.1093/mnras/stz3007](https://doi.org/10.1093/mnras/stz3007)
- Narang, M., Manoj, P., & Ishwara Chandra, C. H. 2021, *Research Notes of the American Astronomical Society*, 5, 158, doi: [10.3847/2515-5172/ac0fe0](https://doi.org/10.3847/2515-5172/ac0fe0)
- Ninan, J. P., Bender, C. F., Mahadevan, S., et al. 2018, in *Society of Photo-Optical Instrumentation Engineers (SPIE) Conference Series*, Vol. 10709, *High Energy, Optical, and Infrared Detectors for Astronomy VIII*, ed. A. D. Holland & J. Beletic, 107092U, doi: [10.1117/12.2312787](https://doi.org/10.1117/12.2312787)

- Nutzman, P., & Charbonneau, D. 2008, *PASP*, 120, 317, doi: [10.1086/533420](https://doi.org/10.1086/533420)
- Parker, E. N. 1958, *ApJ*, 128, 664, doi: [10.1086/146579](https://doi.org/10.1086/146579)
- Parviainen, H. 2016, *PyDE*: v1.5, doi: [10.5281/zenodo.45602](https://doi.org/10.5281/zenodo.45602)
- Paudel, R. R., Gizis, J. E., Mullan, D. J., et al. 2020, *MNRAS*, 494, 5751, doi: [10.1093/mnras/staa1137](https://doi.org/10.1093/mnras/staa1137)
- Pérez-Torres, M., Gómez, J. F., Ortiz, J. L., et al. 2021, *A&A*, 645, A77, doi: [10.1051/0004-6361/202039052](https://doi.org/10.1051/0004-6361/202039052)
- Perryman, M., Hartman, J., Bakos, G. Á., & Lindegren, L. 2014, *ApJ*, 797, 14, doi: [10.1088/0004-637X/797/1/14](https://doi.org/10.1088/0004-637X/797/1/14)
- Pineda, J. S., & Villadsen, J. 2023, *Nature Astronomy*, 7, 569, doi: [10.1038/s41550-023-01914-0](https://doi.org/10.1038/s41550-023-01914-0)
- Pont, F., Husnoo, N., Mazeh, T., & Fabrycky, D. 2011, *MNRAS*, 414, 1278, doi: [10.1111/j.1365-2966.2011.18462.x](https://doi.org/10.1111/j.1365-2966.2011.18462.x)
- Pope, B. J. S., Callingham, J. R., Feinstein, A. D., et al. 2021, *ApJL*, 919, L10, doi: [10.3847/2041-8213/ac230c](https://doi.org/10.3847/2041-8213/ac230c)
- Preusse, S., Kopp, A., Büchner, J., & Motschmann, U. 2005, *A&A*, 434, 1191, doi: [10.1051/0004-6361:20041680](https://doi.org/10.1051/0004-6361:20041680)
- Raghavan, D., McAlister, H. A., Henry, T. J., et al. 2010, *ApJS*, 190, 1, doi: [10.1088/0067-0049/190/1/1](https://doi.org/10.1088/0067-0049/190/1/1)
- Ramsey, L. W., Adams, M. T., Barnes, T. G., et al. 1998, in *Society of Photo-Optical Instrumentation Engineers (SPIE) Conference Series*, Vol. 3352, *Advanced Technology Optical/IR Telescopes VI*, ed. L. M. Stepp, 34–42, doi: [10.1117/12.319287](https://doi.org/10.1117/12.319287)
- Rasio, F. A., Tout, C. A., Lubow, S. H., & Livio, M. 1996, *ApJ*, 470, 1187, doi: [10.1086/177941](https://doi.org/10.1086/177941)
- Reiners, A., & Christensen, U. R. 2010, *A&A*, 522, A13, doi: [10.1051/0004-6361/201014251](https://doi.org/10.1051/0004-6361/201014251)
- Ricker, G. R. 2015, in *AAS/Division for Extreme Solar Systems Abstracts*, Vol. 47, *AAS/Division for Extreme Solar Systems Abstracts*, 503.01
- Rivera, E. J., Lissauer, J. J., Butler, R. P., et al. 2005, *ApJ*, 634, 625, doi: [10.1086/491669](https://doi.org/10.1086/491669)
- Saur, J., Grambusch, T., Duling, S., Neubauer, F. M., & Simon, S. 2013, *A&A*, 552, A119, doi: [10.1051/0004-6361/201118179](https://doi.org/10.1051/0004-6361/201118179)
- Saur, J., Willmes, C., Fischer, C., et al. 2021, *A&A*, 655, A75, doi: [10.1051/0004-6361/202040230](https://doi.org/10.1051/0004-6361/202040230)
- Shkolnik, E., Walker, G. A. H., Bohlender, D. A., Gu, P. G., & Kürster, M. 2005, *ApJ*, 622, 1075, doi: [10.1086/428037](https://doi.org/10.1086/428037)
- Sozzetti, A., Casertano, S., Lattanzi, M. G., & Spagna, A. 2001, *A&A*, 373, L21, doi: [10.1051/0004-6361:20010788](https://doi.org/10.1051/0004-6361:20010788)
- Sozzetti, A., Giacobbe, P., Lattanzi, M. G., et al. 2014, *MNRAS*, 437, 497, doi: [10.1093/mnras/stt1899](https://doi.org/10.1093/mnras/stt1899)
- Stassun, K. G., Oelkers, R. J., Pepper, J., et al. 2018, *AJ*, 156, 102, doi: [10.3847/1538-3881/aad050](https://doi.org/10.3847/1538-3881/aad050)
- Stassun, K. G., Oelkers, R. J., Paegert, M., et al. 2019, *AJ*, 158, 138, doi: [10.3847/1538-3881/ab3467](https://doi.org/10.3847/1538-3881/ab3467)
- Stefansson, G., Harty, F., Robertson, P., et al. 2016, *ApJ*, 833, 175, doi: [10.3847/1538-4357/833/2/175](https://doi.org/10.3847/1538-4357/833/2/175)
- Stefansson, G., Mahadevan, S., Maney, M., et al. 2020, *AJ*, 160, 192, doi: [10.3847/1538-3881/abb13a](https://doi.org/10.3847/1538-3881/abb13a)
- Stock, S., Kemmer, J., Reffert, S., et al. 2020, *A&A*, 636, A119, doi: [10.1051/0004-6361/201936732](https://doi.org/10.1051/0004-6361/201936732)
- Trigilio, C., Biswas, A., Leto, P., et al. 2023, *arXiv e-prints*, arXiv:2305.00809, doi: [10.48550/arXiv.2305.00809](https://doi.org/10.48550/arXiv.2305.00809)
- Turnpenney, S., Nichols, J. D., Wynn, G. A., & Burleigh, M. R. 2018, *ApJ*, 854, 72, doi: [10.3847/1538-4357/aaa59c](https://doi.org/10.3847/1538-4357/aaa59c)
- Udry, S., Mayor, M., Delfosse, X., Forveille, T., & Perrier-Bellet, C. 2000, *IAU Symposium*, 200, 158
- Van Der Walt, S., Colbert, S. C., & Varoquaux, G. 2011, *ArXiv e-prints*. <https://arxiv.org/abs/1102.1523>
- Vedantham, H. K., Callingham, J. R., Shimwell, T. W., et al. 2020, *Nature Astronomy*, 4, 577, doi: [10.1038/s41550-020-1011-9](https://doi.org/10.1038/s41550-020-1011-9)
- Vidotto, A. A. 2021, *Living Reviews in Solar Physics*, 18, 3, doi: [10.1007/s41116-021-00029-w](https://doi.org/10.1007/s41116-021-00029-w)
- Vidotto, A. A., Fares, R., Jardine, M., et al. 2012, *MNRAS*, 423, 3285, doi: [10.1111/j.1365-2966.2012.21122.x](https://doi.org/10.1111/j.1365-2966.2012.21122.x)
- Villadsen, J., & Hallinan, G. 2019, *ApJ*, 871, 214, doi: [10.3847/1538-4357/aaf88e](https://doi.org/10.3847/1538-4357/aaf88e)
- Weisskopf, M. C., Tananbaum, H. D., Van Speybroeck, L. P., & O'Dell, S. L. 2000, in *Society of Photo-Optical Instrumentation Engineers (SPIE) Conference Series*, Vol. 4012, *X-Ray Optics, Instruments, and Missions III*, ed. J. E. Truemper & B. Aschenbach, 2–16, doi: [10.1117/12.391545](https://doi.org/10.1117/12.391545)
- Winn, J. N. 2022, *AJ*, 164, 196, doi: [10.3847/1538-3881/ac9126](https://doi.org/10.3847/1538-3881/ac9126)
- Winters, J. G., Irwin, J., Newton, E. R., et al. 2018, *AJ*, 155, 125, doi: [10.3847/1538-3881/aaa65](https://doi.org/10.3847/1538-3881/aaa65)
- Wood, B. E., Müller, H.-R., Redfield, S., et al. 2021, *ApJ*, 915, 37, doi: [10.3847/1538-4357/abfda5](https://doi.org/10.3847/1538-4357/abfda5)
- Wright, N. J., & Drake, J. J. 2016, *Nature*, 535, 526, doi: [10.1038/nature18638](https://doi.org/10.1038/nature18638)
- Wright, N. J., Newton, E. R., Williams, P. K. G., Drake, J. J., & Yadav, R. K. 2018, *MNRAS*, 479, 2351, doi: [10.1093/mnras/sty1670](https://doi.org/10.1093/mnras/sty1670)
- Yee, S. W., Petigura, E. A., & von Braun, K. 2017, *ApJ*, 836, 77, doi: [10.3847/1538-4357/836/1/77](https://doi.org/10.3847/1538-4357/836/1/77)
- Zarka, P. 2007, *Planet. Space Sci.*, 55, 598, doi: [10.1016/j.pss.2006.05.045](https://doi.org/10.1016/j.pss.2006.05.045)
- Zarka, P., Cecconi, B., & Kurth, W. S. 2004, *Journal of Geophysical Research (Space Physics)*, 109, A09S15, doi: [10.1029/2003JA010260](https://doi.org/10.1029/2003JA010260)

- Zarka, P., Treumann, R. A., Ryabov, B. P., & Ryabov, V. B. 2001, *Ap&SS*, 277, 293,
doi: [10.1023/A:1012221527425](https://doi.org/10.1023/A:1012221527425)
- Zechmeister, M., Reiners, A., Amado, P. J., et al. 2018, *A&A*, 609, A12, doi: [10.1051/0004-6361/201731483](https://doi.org/10.1051/0004-6361/201731483)